

Human Serum Albumin Loaded with Fatty Acids Reveals Complex Protein–Ligand Thermodynamics and Boleadora-Type Solution Dynamics Leading to Gelation

Jörg Reichenwallner, Sebastian Michler, Christian Schwieger, and Dariush Hinderberger*

Cite This: *J. Phys. Chem. B* 2025, 129, 3571–3589

Read Online

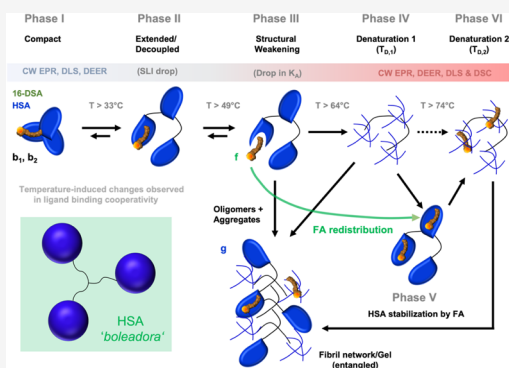
ACCESS |

Metrics & More

Article Recommendations

Supporting Information

ABSTRACT: Using an electron paramagnetic resonance (EPR) spectroscopic strategy that has been developed for core–shell polymers, the complexity of the binding of fatty acids to human serum albumin (HSA) is characterized in detail. We unravel the internal dynamics of HSA solutions with fatty acids by applying continuous wave EPR (CW EPR) from which we derive a consistent thermodynamic interpretation about fatty acid interactions with HSA in the investigated temperature range of 5–97 °C. Additionally, data from CW EPR are corroborated by dynamic light scattering (DLS), differential scanning calorimetry (DSC) and nanoscale distance measurements using double electron–electron resonance (DEER) spectroscopy. We discuss our data in light of decades of biophysical studies on albumin and aim at drawing a complete functional and dynamic picture of HSA “at work”. This picture suggests that HSA is built from modular, rotationally decoupled domains that resemble an entangled three-piece *boleadora* in solution.



INTRODUCTION

Many types of serum albumins, the major transport proteins in the blood of mammals, have been extensively studied in protein biophysical chemistry since the 1950s.^{1–3} Due to their high abundance (near mM concentration in blood) and availability, albumins of different species mainly bovine serum albumin (BSA) and to a much lesser degree human serum albumin (HSA) have been used as model proteins for ligand binding studies.^{4,5} Although BSA and HSA share high sequence identity and similar X-ray crystal structures, they cannot be considered identical. Recent studies, including our own, have highlighted the unique individual properties of these proteins.^{6–8} Continuous wave electron paramagnetic resonance (CW EPR) spectroscopy has been used from early on to study fatty acid (FA)–albumin interactions. However, due to their enormous complexity, CW EPR spectra of spin-labeled fatty acids (SLFA) bound to albumin were predominantly treated phenomenologically in the 1970s and 1980s.^{9–16} Most of these approaches studied uptake capabilities and ligand interactions of albumin and paramagnetic FAs. Beyond these rather phenomenological studies, rigorous, simulation-based dynamic analysis of albumin associated with a variety of SLFAs were reported by Shenkar et al.¹⁷ and in an earlier attempt by Gaffney and McConnell.¹⁸ In recent years, spectral simulations of spin-probed or spin-labeled albumin samples have resurged, mainly due to broad accessibility of powerful spectral simulation tools for CW EPR.^{8,19–36} The main information content from CW EPR spectra on FA-probed HSA and their rigorous simulations is,

first, the ¹⁴N-hyperfine coupling (isotropic a_{iso} or hyperfine coupling tensor component A_{zz}) to the electron spin density that gives insights into the environmental polarity with a lower a_{iso} value indicating nonpolar and a higher a_{iso} value a more polar environment. A second, even more important aspect that can be investigated is rotational diffusion, which gives us information on the motional freedom of a nitroxide (ligand).³ The latter is usually described by the isotropic rotational correlation time τ_C . Standard CW EPR experiments on nitroxides are sensitive to changes in a_{iso} values from 40 to 48 MHz and rotational correlation times in the range from about 10 to 50.000 ps (50 ns). A scheme of FA alignment in HSA is shown in Figure 1A.

Here, we aim at crafting a complete model of the functional (solution) structure and dynamics of albumin as derived from its ligand binding. We will discuss the work presented here against the large body of remarkably inconsistent EPR-spectroscopic and other biophysical data to construct a model that robustly fits all major findings so far. In particular, in the pertinent literature one finds a range of overall 2–5 spectral components of SLFAs bound to albumin.^{17,19,27} This may be mainly due to problems with separability of the individual spectral components.³⁷

Received: December 30, 2024

Revised: March 11, 2025

Accepted: March 13, 2025

Published: March 26, 2025



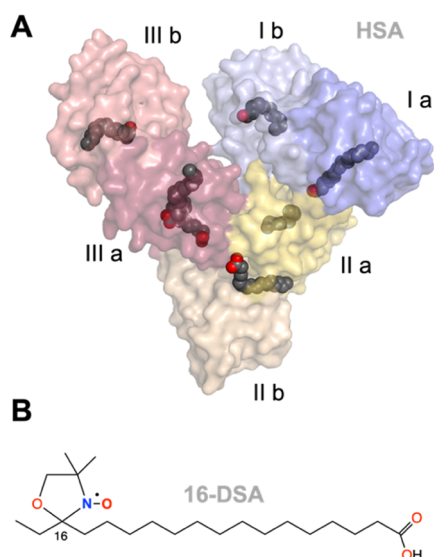


Figure 1. Structures of HSA and 16-DSA. (A) Crystal structure (PDB 1e7i) of HSA cocrystallized with seven stearic acid molecules.⁴⁵ The oxygen atoms of the FA carboxylic acid head groups are displayed in red. (B) Chemical structure of the paramagnetic EPR-active ligand 16-DSA.

Building on an analysis developed for characterization of FA uptake in core–shell polymeric systems,^{38,39} we here transfer this mathematical treatment to derive a physical picture of how

FA assembly in HSA affects the protein's structure and dynamics.

It has already been shown that albumin also exhibits two types of immobilized spectral components from the stearic acid derivative 16-DSA (16-DOXYL stearic acid, see Figure 1B) that are commonly assigned to weak and strong binding sites.^{20,27,31,32} As these components change their spectral fractions with temperature and FA loading, it was proposed that the occupation of weak and strong binding sites changes due to an intra-albumin migration mechanism with an apparent activation energy of 26.8 kJ/mol for HSA and 35.2 kJ/mol for BSA.²⁰ EPR spectroscopic thermal denaturation studies based on spectral simulation of both, SLFA-probed HSA and BSA, have already been conducted in the range from 20 to 50 °C,^{20,31} however, well below their individual denaturation temperature T_D . This is largely due to the impressive thermostability of HSA which is based on its highly conserved 17 disulfide bridges.^{4,40}

In this study, we mainly report EPR-spectroscopic data of temperature-dependent HSA-FA binding and simultaneous HSA denaturation, allowing us to derive a picture of the local dynamics and global structure of the protein. To this end, CW EPR and double electron–electron resonance (DEER) data on HSA^{3,6,41–44} are complemented with other techniques such as differential scanning calorimetry (DSC) and dynamic light scattering (DLS) to reveal a solution-based dynamic model of albumin interacting with SLFA ligands in the temperature range of liquid water. Several well-known phenomena are recapitulated, discussed and integrated to corroborate a model reflecting

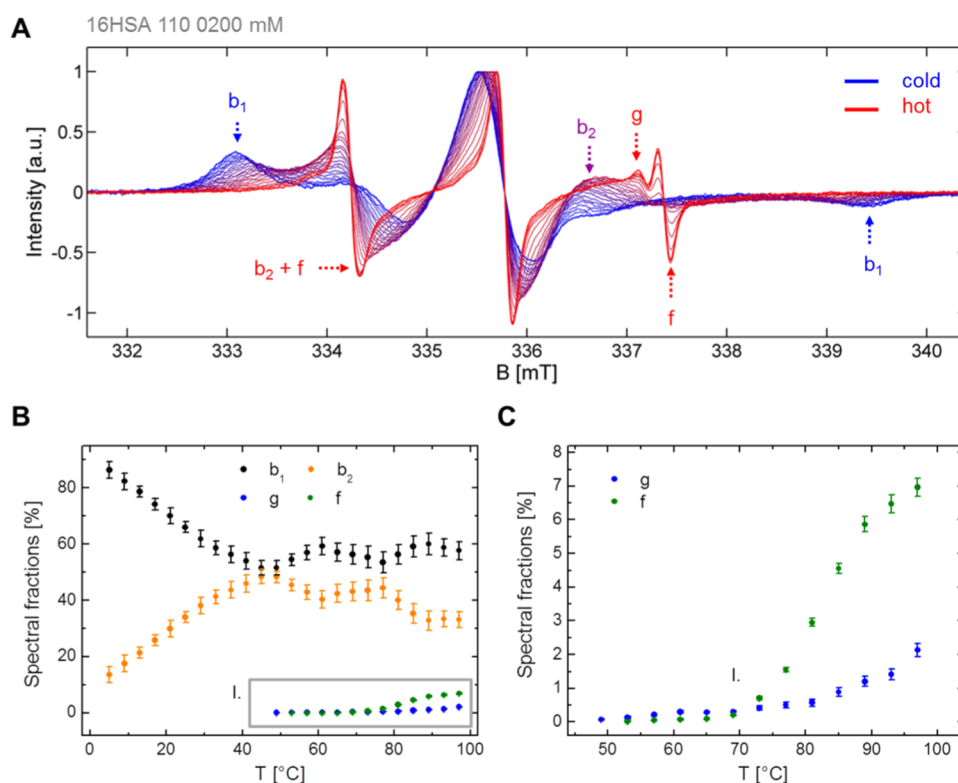


Figure 2. Temperature-dependent CW EPR spectra of 16-DSA interacting with HSA. Spectra were measured in the temperature range from 5 to 97 °C in steps of $\Delta T = 4$ °C. The exact 16-DSA loading ratio of HSA is 1.13:1.00 ($c_{\text{HSA}} = 0.18$ mM). (A) CW EPR spectra of 16-DSA interacting with HSA. The most prominent spectral features of dynamic fractions f , b_1 , b_2 and g are highlighted. The lowest (dark blue) and the highest (dark red) temperature curves are shown in bold to create an envelope effect. (B) Spectral fractions from simulations of 16-DSA interacting with HSA. Immobilized fractions are shown in black (b_1) and orange (b_2), whereas hydrogel-like fractions (g) are shown in blue and free fractions (f) are shown in green. (C) A magnification of inset I in (B) is shown. All error margins have been determined from individual spectral simulations.

that HSA in solution consists of modular, rotationally decoupled domains resembling a self-capturing boleadora-type domain alignment.

MATERIALS AND METHODS

Materials. Lyophilized powder of HSA (>95%, Calbiochem), 16-DSA (Sigma-Aldrich) and 87 wt % glycerol (ACROS Organics) were used without further purification. The 0.137 M Dulbecco Phosphate-Buffered Saline (DPBS) buffer⁴⁶ with pH 7.4 was prepared according to the procedure described in the Supporting Information S1.

Sample Preparation. All experiments were conducted on HSA solutions loaded with 16-DSA equivalents of moderately varying ratios. Regardless of the applied method the protein concentration was kept constant at about $c_{\text{HSA}} = 0.18$ mM. As the stability of HSA is also dependent on its concentration, only the concentration of 16-DSA was varied by default throughout the whole study. All sample volumes were adjusted for device-specific requirements ranging from about 0.01–1.00 mL. HSA was dissolved in 0.137 M DPBS buffer pH 7.4 to a final stock concentration of 1 mM. Upon addition of an 8 mM stock solution 16-DSA dissolved in 0.1 M KOH the solution gained a slight alkaline pH change being compensated by titrating with appropriate alkaline and acidic 0.12 M DPBS-buffers (range pH 1–13) containing varying amounts of HCl and NaOH, so that final physiological values of $\text{pH } 7.42 \pm 0.06$ could be comfortably adjusted for all samples. The exact amounts of added 16-DSA was determined by double integration of corresponding CW EPR spectra throughout.

Temperature steps for HSA denaturation with CW EPR (Figure 2) were set to $\Delta T = 4$ K and the molar ratio of HSA to 16-DSA was 1.00 to 1.13 with a 16-DSA concentration of $[L]_t = 204 \pm 6$ μM . About 15 μL of the final solutions were filled into appropriate EPR-silent capillaries (BLAUBRAND IntraMARK) for the experiment.

In order to determine temperature dependent association constants K_{A_j} and number of equivalent binding sites $N_{E,j,p}$ from CW EPR-based Scatchard plots, the molar ratios of HSA to 16-DSA were varied in the range from 0 to 8 equiv at pH 7.4 to prevent ligand micelle formation.^{13,47} The critical micelle concentration (CMC) of 16-DSA was determined as (285 ± 29) μM via CW EPR spectroscopy (see Supporting Information S2). Micelles are thus expected when the free ligand concentration $[L]_f$ would exceed about 0.3 mM. This unwanted phenomenon was successfully prevented in all recorded CW EPR spectra. Likewise, for DEER spectroscopy it is crucial that no micelle-based exchange interaction can occur between proximal nitroxide moieties to maximize dipolar evolution time and thus achieve maximum data quality.

Unlike in CW EPR experiments of this study, all DEER samples were additionally equipped with 20% v/v glycerol to prevent crystallization upon freezing. The same accounts for individually prepared samples that were used in the 16-DSA loading study with DEER for extraction of reference data for the DEER temperature denaturation. For temperature denaturation as monitored by DEER, a single sample was prepared as a 1 mL stock solution at pH 7.38 that was aliquoted into 0.05 mL fractions, so that each sample contains identical ingredients and conditions. All spin probed HSA samples for DEER spectroscopy were filled into 3 mm outer diameter quartz tubes (Heraeus Quarzschmelze) and the aliquots were additionally incubated for 5 min at individual temperatures in the range from $9 < T < 81$ °C. The incubation temperatures for DEER experiments were

chosen to coincide with temperatures in all other experiments and were also conducted in steps of $\Delta T = 4$ K in a water bath that was set up with ultrapure water (Milli-Q) in Eppendorf reaction tubes being preheated for sufficient time in an Eppendorf Thermomixer C (~5 min for each temperature). Directly after temperature incubation, the samples were shock frozen in liquid nitrogen-cooled 2-methylbutane (Sigma-Aldrich) for subsequent DEER measurements. The samples for mere 16-DSA loading studies with DEER were conveniently just shock frozen from room temperature without further treatment.

EPR Spectroscopy. CW EPR Experiments. A Miniscope MS400 (Magnetech GmbH) benchtop spectrometer was employed for X-band CW EPR measurements operating at a microwave frequency of 9.4 GHz. All measurements were performed in the temperature range of $5 < T < 97$ °C utilizing modulation amplitudes of 1 G during a field sweep of 15 mT with an incident microwave power in the range of 3.16 mW. For precise temperature adjustments (intrinsic error is about 0.3 K) a temperature controller (Magnetech Temperature Controller H03) was used. EPR spectra for 16-DSA-based temperature response curves of HSA were recorded in steps of $\Delta T = 4$ K with a precautionary incubation time for each temperature step of about 2–5 min. The microwave frequency was recorded with a frequency counter (RACAL-DANA, model 2101).

DEER Experiments. The four-pulse DEER sequence:^{48,49} $\pm (\pi/2)_{\text{obs}} - \tau_1 - (\pi)_{\text{obs},1} - t_d - (\pi)_{\text{pump}} - \tau_2 - (\pi)_{\text{obs},2} - \tau_2 - \text{RE}$ was used to obtain dipolar time evolution data from paramagnetic 16-DSA spin probes interacting with HSA at X-band frequencies of 9.1–9.4 GHz with a BRUKER Elexsys E580 spectrometer equipped with a BRUKER Flexline splitting resonator ER4118X-MS3. The temperature was set to $T = 50$ K by cooling with a closed cycle Helium cryostat (ARS AF204, customized for pulse EPR, ARS, Macungie, PA) and the resonator was overcoupled to ca. $Q \approx 100$. The pump pulse position after the first observer π -pulse t_d was typically incremented for N_t timesteps of $\Delta t = 8$ ns in the range $\tau_1 + \tau_2 - 2t_d$ whereas τ_1 and τ_2 were kept constant. Proton modulation was averaged out by summation of eight time traces of variable τ_1 starting with $\tau_{1,1} = 200$ ns, incrementing by $\Delta\tau_1 = 8$ ns and ending up at $\tau_{1,8} = 256$ ns. Additionally, a 2-step phase cycle (\pm) was applied to the first $\pi/2$ pulse of the observer frequency for canceling out receiver offsets and unwanted echoes. The pump frequency ν_{pump} was set to the maximum of the field swept electron spin echo (FS ESE)-detected spectrum. The observer frequency ν_{obs} was set to $\nu_{\text{pump}} + \Delta\nu$ with $\Delta\nu$ being in the range of 65 MHz and therefore coinciding with the low field local maximum of the nitroxide ESE spectrum. The observer pulse lengths for each DEER experiment were set to 32 ns for both $\pi/2$ - and π -pulses (with varying intensity) and the pump pulse length was 12 ns.

EPR Data Analysis. All EPR data have been evaluated in MATLAB 2021b. Spectral simulations of spin probed HSA samples for temperature denaturation and Scatchard plots were conducted with the MATLAB-based Easyspin 6.0.0 software package.⁵⁰ All corresponding MATLAB codes have been optimized for 2- to 4-component nitroxide spectra. Individual subspectra were double-integrated to extract the spectral fraction concentrations $[L]_t \phi_{ij}$ ($[L]_t$ = total ligand (SLFA) concentration, ϕ_{ij} = temperature-dependent spectral fraction) of corresponding dynamic populations for subsequent thermodynamic analysis. For an appropriate starter set of simulation parameters and the simulation approach the reader is referred to Table S1. All spectral simulations can be found in Figures S3 and

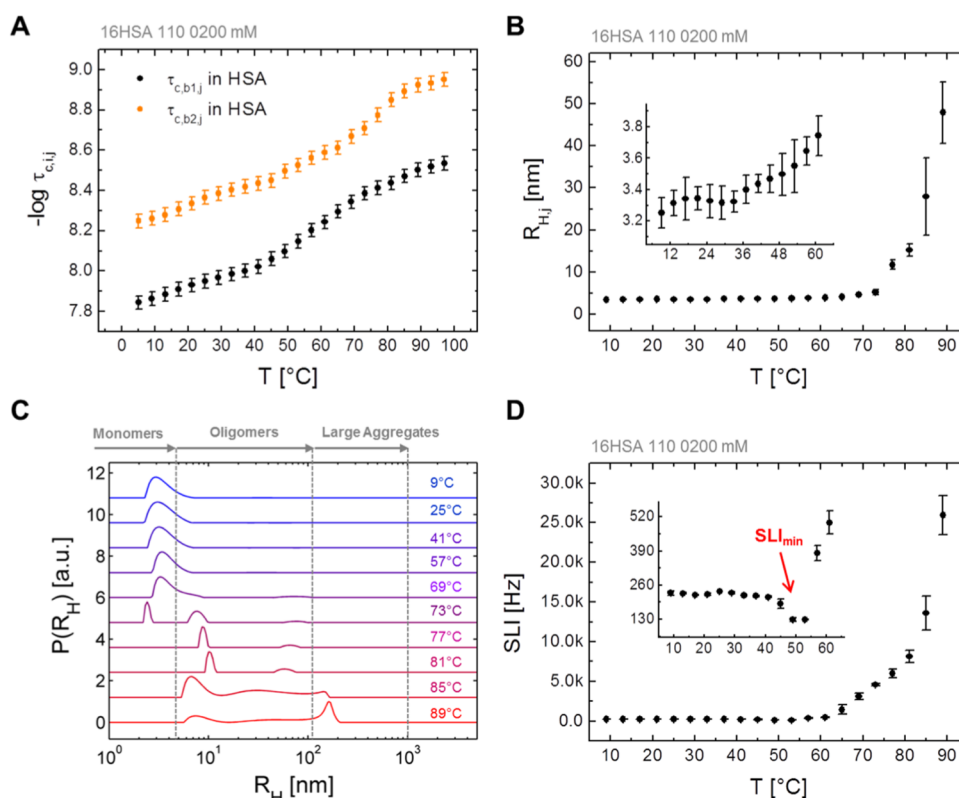


Figure 3. Temperature-induced changes in spin probe and protein dynamics. Comparison of CW EPR and DLS data from a 16-DSA-probed HSA solution in the temperature range from 5 to 97 °C (9 to 89 °C for DLS data) in steps of $\Delta T = 4$ K. (A) Semilogarithmic plot of the temperature-dependent rotational correlation times $\tau_{c,ij}$ from CW EPR of spectral components b_1 (black) and b_2 (orange) of 16-DSA interacting with HSA. Error margins were estimated from spectral simulations to be about 8%. (B) The temperature-dependence of the main hydrodynamic radii R_H is shown as detected in DLS experiments. Error bars are given as the fluctuation about the mean values of individual measurements at a constant temperature. (C) The temperature-dependent particle size distributions $P(R_H)$ in spin probed HSA solutions are given here. Three different regimes are highlighted comprising monomers from 9 to 57 °C, oligomers above 70 °C and larger aggregates above 80 °C. (D) The scattered light intensity (SLI) is given as a count rate (in Hz) from temperature-dependent DLS experiments on 16-DSA-probed HSA with a clear minimum at temperatures between 45 and 57 °C (SLI_{min}). All experiments were performed at pH 7.4 with 1:1 nominal equivalents of 16-DSA to HSA at 0.2 mM.

S4 in the SI. Fit parameters that were obtained from temperature-dependent Scatchard plots are presented in Tables S2 and S3. Scatchard plots were analyzed according to strategies presented in^{8,28,38} using linear regressions as well as the Rosenthal method.⁵¹ Temperature-dependent and ligand loading-dependent $\ln K_{IC,j}$ values were also obtained in the course of Scatchard plot evaluation. These curves were reconstructed with exponential fit curves. The cooperativity test for both Scatchard plots (see Figure S5) was conducted as described in refs 8 and 28.

Thermodynamic analyses from CW EPR spectral simulations in this study are largely adopted from the strategies described in³⁹ with several adjustments. All physical quantities that emerge from equilibrium constants $K_{A,j}$ and $K_{IC,j}$ have been calculated with fit parameters that were obtained from a sigmoidal fit curve $\ln K_{A,j}$ in eq 1 and a homewritten combination of exponential and double sigmoidal Boltzmann curve regression ($\ln K_{IC,j}$ in eq 3) in Microcal Origin (see Table S4). Fit parameters from the aforementioned curve regressions in Origin were incorporated in the homewritten MATLAB codes that generate appropriate energy plots (Table S5). All corresponding thermodynamic functions for $\ln K_{IC,j}$, $\Delta G_{IC,j}^\circ$, $\Delta H_{IC,j}^\circ$, $\Delta S_{IC,j}^\circ$ and $\Delta C_{p,IC,j}^\circ$ in this graph were computed in a quasi-continuous 500 point grid corresponding to about 0.19 K temperature resolution. Derivations of the expressions given in eqs 5–8 are explicitly shown in the Supporting Information. Characteristic temper-

atures as $T_{AH,i}$, $T_{AD,i}$ and $T_{H,i}$ were obtained from relations given in³⁹ and are shown in Figure S6. Due to the complexity in $\Delta C_{p,IC,j}^\circ$ the apolar hydration temperature was introduced in analogy to $T_{AD,i}$ at zero-crossings with increasing temperature.

The raw DEER time domain data as shown in Figure S7 were processed with the MATLAB-based program package Deer-Analysis2019.⁵² For the DEER-derived 16-DSA loading study, all background dimensionalities were set to $D = 3.74$ throughout. These data sets serve as a reference for calculations of the average number of spins from the distribution shape ($N_{p(r)}$). The derivation of an empiric equation that enables to pursue this strategy is based on an exponential fit curve to $\ln P_{AB}(r)$; these data are given in the Supporting Information (eq S41). As no spin dilution was applied to these samples, a Langmuir power law could be used for reproducing the modulation depths (Δ) best when 16-DSA loading to HSA varies in the range from about 0.8–6.2 equiv. Similarly, an empirical relation was derived in the Supporting Information that facilitates prediction of the average number of coupled spins based on the modulation depth at room temperature (N_{Δ} , see eq 11). Due to the change in shape and compactness of HSA with temperature, this approach is preliminary discouraged as the modulation depth experiences additional modification in this respect. All DEER time traces that were obtained from temperature-incubated samples were background-corrected with adjustable spin distribution dimensionalities ranging from

$2.00 < D < 3.76$. These dimensionalities were obtained in a comparative iterative global analysis of all data sets prior to the final Tikhonov regularization procedure. All first moments $\langle r \rangle$ of individual distance distributions $P(r)$ were plainly obtained from the DeerAnalysis result files.

DLS Measurements. All DLS data were obtained with an ALV-NIBS high performance particle sizer (HPPS) equipped with an ALV-5000/EPP Multiple Tau Digital Correlator (ALV-Laser Vertriebsgesellschaft m. b. H.). The ALV-NIBS device facilitates HeNe-LASER irradiation with a typical wavelength of $\lambda = 632.8$ nm and a 3 mW output power source. Count rates were recorded in a backscattering detection angle of 173° relative to the incident monochromatic light. The sample cell temperatures were adjusted in the range of $9 < T < 89^\circ\text{C}$ in steps of $\Delta T = 4$ K by a Peltier temperature control unit. HSA temperature denaturation was conducted on an individual sample in 1.5 mL PMMA semimicro cuvettes (BRAND). For sustaining comparability, a nominal 1-to-1 ratio of 16-DSA was used to equip the protein with the same FA content as in respective CW EPR experiments, well below the CMC = (0.285 ± 0.029) mM. A sample volume of 0.4–0.6 mL was filtered through Rotilabo cellulose acetate (CA) syringe filters with a pore size of $0.2 \mu\text{M}$ (Rotilabo, Carl Roth GmbH + Co. KG) in order to minimize sample adhesion and therefore protein concentration loss.

HSA particle size data were extracted from the intensity correlation functions by a $g_2(t)$ -DLS exponential and a mass weighted regularized fit in the ALV-NIBS software v.3.0 utilizing the CONTIN algorithm. The refractive index was assumed to be constant at $n_{\text{H}_2\text{O}} = 1.332$ for all temperatures (and $\lambda = 632.8$ nm), the water (DPBS buffer) viscosity was corrected for each applied temperature assuming that $\eta_0 = 1.002$ mPa·s at $T = 20^\circ\text{C}$. Deviations in true viscosities from calculated values that are induced by the intrinsic viscosity of HSA are considered as marginal and do not exceed +7.7% at $c_{\text{HSA}} = 0.18$ mM = 12.0 mg/mL within $5^\circ\text{C} < T < 45^\circ\text{C}$. Each sample was measured at least four times at the same temperature for 30 s and was averaged at least over three individual values. The mean values $R_{\text{H},j}$ of the most prominent size peaks and their statistical fluctuations are given as the standard deviation as depicted in the error bars in Figure 3. The duration of the whole heating procedure was about 8–9 h.

Differential Scanning Calorimetry (DSC) Measurements. All DSC experiments and data evaluations were performed using a Microcal VP-DSC device (MicroCal Inc.). In all experiments a heating rate of 0.25 K/min was used. Data were recorded with a time resolution of 4 s in the temperature range of $5\text{--}95^\circ\text{C}$ that covers the decisive regions of the corresponding EPR experiments. Two consecutive up and down scans were performed for each sample. However, due to irreversible gelation of the HSA-containing samples at high temperature, only the first thermogram is presented and evaluated. In scan 2–4 only residual heats could be detected and data are therefore not shown.

All 16-DSA-probed HSA solutions were loaded to the sample cell and for comparability the HSA concentration was again set to $c_{\text{HSA}} = 0.18$ mM. The ligand-to-protein ratio was varied in the range from about 0–8 equiv, so that altogether eight thermograms were obtained. Pure, degassed DPBS buffer was loaded into the reference cell. Therefore, from all presented thermograms of 16-DSA-probed HSA samples a buffer/buffer reference, as well as a thermogram of pure 16-DSA was subtracted before normalizing $\Delta C_{\text{P,HSA}}$ to the HSA concen-

trations. Afterward, a cubic baseline was subtracted manually. Data processing was performed with the DSC module for Origin software (MicroCal Inc.). The obtained thermograms were fitted with two Gaussian curves in order to deconvolute both overlapping transitions ($T_{\text{D},1}$ and $T_{\text{D},2}$). The midpoints of the obtained Gaussians were finally used as transitions temperatures for the two HSA species and are given in the scheme according to Shrake and Ross.^{53,54} A brief rationalization of these results is given in the Supporting Information.

General Remarks. For simplicity temperature dependent variables will have a j as index representing the temperature as $j = T [^\circ\text{C}]$, i denotes the dynamic regime (b_1, b_2, f, g) or any running number, k when different samples were considered and p to differentiate different phases in a Scatchard plot. All other parameters and indices are explained in the appropriate sections of the main text, the Supporting Information, or in Reichenwallner et al.³⁹ The abbreviation “16HSA 110 0200 mM” stands for a standard sample that is composed of 16-DSA-probed HSA in a ratio of 1:1 equiv of 0.2 mM.

RESULTS AND DISCUSSION

Temperature-Dependent Dynamic Regimes of 16-DSA in HSA Solutions. The temperature dependence of FA binding to HSA, as seen from the FAs' points of view, generates CW EPR spectra that consist of a superposition of different spectral species (Figure S2 and Table S1 in the Supporting Information). Classical empirical approaches in EPR spectroscopy, such as measuring line amplitude ratios¹⁰ may not fully capture the complexity of thermal denaturation processes. Therefore, we here use an iterative, manual and global simulation procedure as already established for amphiphilic core–shell polymers.^{8,38,39}

EPR spectra of 16-DSA in HSA solutions were investigated in the temperature range from 5 to 97°C . As known from earlier studies, several dynamic regimes of 16-DSA emerge when this ligand is co-dissolved with HSA. The applied FA loading ratio of 1.13:1.00 at an HSA concentration of 0.18 mM was chosen to be below the critical micellar concentration (CMC) of 16-DSA at all investigated temperatures ($c_{16\text{-DSA}} < \text{CMC} = 0.285$ mM, see Supporting Information S2). This generally simplifies spectral simulation procedures, although still up to four different subspectra can be identified (Figure 2), however, without micelle-based spectral contributions.

Exemplary, simulation parameters for spectra at three characteristic temperatures (25, 37, and 97°C) are given in Table S1 and all simulations in the whole temperature range are depicted in Figure S3

16-DSA in HSA solutions at ambient temperatures exhibits two immobilized fractions b_1 and b_2 , similar to what can be observed for hydrophobic core – hydrophilic shell polymers in ref 38. A complete set of recorded spectra and all spectral fractions of the simulated species in the full temperature range are presented in Figure 2, where b_1 appears to be the stronger immobilized spectral component while b_2 shows slightly higher dynamics.

Above $\sim 50^\circ\text{C}$, additional free (f) and hydrogel-like fractions (g)^{7,43,55} are observable, leading to significantly more complex spectra at higher temperatures. The combined b_1 and b_2 fractions comprise 100% of HSA spectra below 50°C and always exceed 90% of the spectral fraction ($\phi > 0.9$) above this temperature. These two spectral components exhibit a highly non-trivial temperature development above 50°C that will be explicitly discussed below.

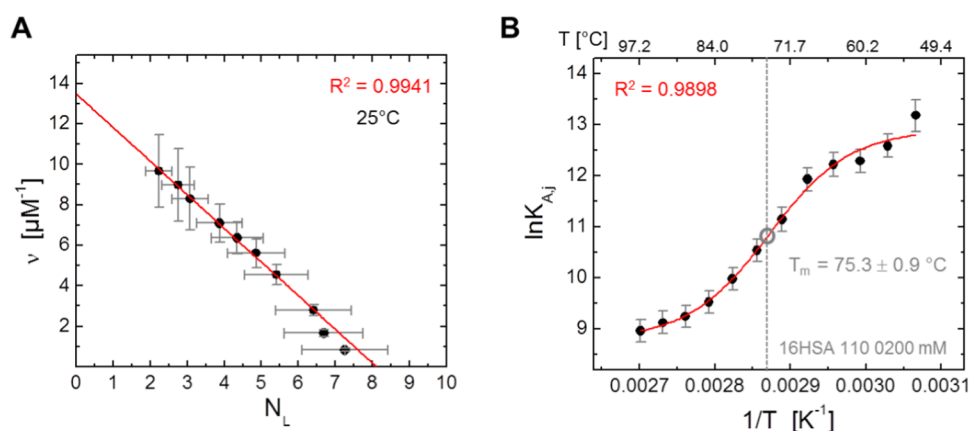


Figure 4. 16-DSA binding affinity and capacity of HSA. (A) Scatchard plot of 16-DSA interacting with HSA at 25 °C (black, full circles) with linear fit (red). The Scatchard plot was constructed in the loading ratios from 2:1 to 8:1. (B) van't Hoff plot of the association constant K_{A_j} is shown that can be constructed from free (f) and bound (b_1, b_2, g) spectral fractions in Figure 2C for $T \geq 53$ °C. A sigmoidal Boltzmann fit curve is shown together with the midpoint temperature T_m ($=\alpha_3^{-1}$, see eq 1). The ligand-to-protein ratio for the van't Hoff plot is 1.13:1.00 at 0.18 mM equivalents. The quality (R^2) of respective fit curves is very high and given as red insets.

The b_1 fraction remains above and b_2 below 50% at all temperatures. The characteristic a_{iso} value as a measure of the environmental polarity for b_1 and b_2 is 42.93 MHz for 25 °C as it was also found by Ge et al. for BSA¹⁷ and decreases to 42.33 MHz (Table S1) at 97 °C. The free (f) fraction starts appearing at 53 °C and shows a sigmoidal increase to about 7.0% at 97 °C. The very hydrophobic, hydrogel-like spectral component g with an a_{iso} value of 40.20 MHz is found above 50 °C but only becomes directly discernible well above 70 °C and reaches a maximum value of 2.1% at 97 °C. It is known that HSA forms ordered macroscopic gel-structures by fibrillation at defined temperatures, pH, osmolality and protein concentrations giving fibrils of 15–30 nm in diameter and 0.1–2.0 μm in length.⁵⁶ We recently reported a thorough physicochemical characterization of the formation of these gel-states from aqueous solutions of HSA and BSA⁷ and have further characterized^{7,55} and developed these gel-state properties since then (see, e.g., ref 57). This gel-state was also found in amphiphilic core–shell polymers.³⁸

When plotting the temperature-dependent τ_c values in a semilogarithmic fashion, the $-\log \tau_c$ curves for spectral components b_1 and b_2 both exhibit a sigmoidal shape (Figure 3A). The rotational correlation time ratio $\tau_{c,b1}/\tau_{c,b2}$ yields a value of 2.46 ± 0.18 when it is averaged across all temperatures, which is very close to 2.65 as proposed for an interconversion from Brownian to free diffusion (K_{IC}).^{38,39,58,59} While the τ_c values decrease from 14.3 ns (5 °C) to 2.9 ns (97 °C) for component b_1 , τ_c -values of b_2 decrease from 5.7 to 1.2 ns in the same temperature range. The most intriguing feature of the $-\log \tau_c$ curves is that $\tau_{c,b1}$ shows a strong decrease (i.e., $-\log \tau_c$ increase) above 50 °C, while $\tau_{c,b2}$ only significantly decreases above 70 °C. This decrease in τ_c is a direct sign of the structural weakening (finally unfolding) of the protein with increasing temperature. Hence, we detect unfolding by a decrease in ligand immobilization. As established in ref 39, the hydrodynamic properties of FAs in HSA solutions from EPR spectroscopy are now discussed in the light of temperature-dependent DLS experiments (Figure 3B–D).

Structural unfolding of HSA was monitored by plotting hydrodynamic radii R_{H} vs temperature (Figure 3B). While the average particle size in the HSA-16-DSA solutions does not change significantly up to 70 °C, a significant size increase takes place above 75 °C. This is due to the emergence of self-

association of HSA leading to oligomers of about 50–100 nm above 57 °C and even larger aggregates above 81 °C (Figure 3C, $R_{\text{H}} > 100$ nm). Macroscopically, it could be confirmed that the investigated HSA solution indeed forms a gel, as the solutions in the DLS cuvette were completely solidified after the experiments.⁷

Closer examination of the data in the temperature range 9 to 63 °C (see inset in Figure 3B) reveals that the particle size is largely constant at about 3.3 nm in the low temperature range (<40 °C). However, above 45 °C a rather significant particle size increase takes place, still without any larger aggregates appearing. The scattered light intensity (SLI, Figure 3D) was recorded simultaneously and, surprisingly, an identifiable drop in SLI is detected between 45 and 57 °C (SLI_{min}) that can be associated with the dissolution of polymer aggregates in our related study on synthetic amphiphilic core–shell polymers.³⁸ Prior albumin studies attributed this effect to a mere opening of the Cys34 crevice,²⁴ some reversible conformational changes,⁶⁰ or a change in compressibility.⁶¹ According to Curry et al., the three globular albumin domains (I–III) rotate as rigid bodies relative to one another and fatty acids may stitch these domains together like lock pins.⁶² This dynamic feature may also be modified by temperature.

As expected, the SLI significantly increases again above 60 °C, when also an increasing number of larger oligomeric HSA aggregates form. Taken together, these data indicate that HSA undergoes a structural rearrangement from a tight to a loose organization of subdomains at intermediate temperatures (40–60 °C) that finally leads to protein aggregation by mutual domain or chain entanglement. Technically, this drop in SLI around 50 °C can be understood in terms of an opening of globular HSA molecules. In turn, the decrease of τ_c values of the spectral component b_1 (Figure 3A) monitoring the global Brownian diffusion confirm the picture of a structural softening of HSA at about 40–50 °C. The τ_c values of the free diffusion process as monitored by b_2 do not exhibit this decrease to such an extent. This circumstance indicates that the domains harboring the 16-DSA ligand remain largely unaffected up to about 70 °C. All these DLS and EPR data corroborate a temperature-induced rotational decoupling of the three HSA domains, reminiscent of an entangled three-piece *boleadora*, a Pre-Columbian South American throwing weapon with weights

Table 1. Thermodynamic Data from 16-DSA Binding to HSA

T [°C]	$N_{T,j}$	p	$N_{E,j,p}$	$K_{A,j,p}$ [M^{-1}]	$K_{D,j,p}$ [M]	$\Delta G_{A,j,p}^{\circ}$ [kJ/mol]	$C_{j,p}^e$
25 ^a	8.1 ± 0.3			(1.66 ± 0.04) × 10 ⁶	(6.03 ± 0.16) × 10 ⁻⁷	-35.5 ± 0.9	(N.C and -)
37 ^b	9.2 ± 2.9	I	4.0 ± 1.3	(5.40 ± 0.74) × 10 ⁶	(1.85 ± 0.25) × 10 ⁻⁷	-40.0 ± 5.5	(-)
		II	5.2 ± 1.6	(2.50 ± 0.60) × 10 ⁵	(4.00 ± 1.01) × 10 ⁻⁶	-32.0 ± 7.7	(- and +)
97 ^c				(7.84 ± 0.49) × 10 ³	(1.27 ± 0.03) × 10 ⁻⁴	-27.6 ± 8.3	N.A.

^aValues are obtained from the Scatchard plot in Figure 4A. ^bValues are obtained from the Rosenthal analysis that was applied to the Scatchard plot in Figure S5A, here with two Scatchard phases p .⁸ ^cValues are obtained from the van't Hoff plot of $\ln K_A$ in Figure 5B. ^dMolar Gibbs free energy change of ligand association at a given temperature and Scatchard phase p . ^eTemperature-dependent ligand binding cooperativity of Scatchard phases p .

at the ends of three interconnected cords that is used to capture animals by entangling their legs.

Temperature-Dependent Ligand Uptake Capabilities of HSA. The 16-DSA binding capacity has been determined for HSA via a Scatchard plot analysis⁶³ after simulation of CW EPR spectra. The simulated CW EPR spectra can be found in the Supporting Information (Figure S4). Two different temperatures have been chosen to investigate the effect that temperature has on the ligand binding properties, one at room temperature (25 °C) and another one at physiological temperature (37 °C). Both Scatchard plots were constructed for ligand/protein loading ratios from 2:1 to 8:1. At 25 °C a linear plot allows for extracting the number of equivalent binding sites N_E and the association (see eq S5, K_A) or dissociation constant (K_D , see Figure 4A). The Scatchard plot at 25 °C reveals a total number of $N_{T,25} = 8.1 \pm 0.3$ equiv binding sites of HSA for 16-DSA with a dissociation constant of $K_D = (603 \pm 16)$ nM, corresponding to an association constant of $K_A = (1.66 \pm 0.04) \times 10^6 M^{-1}$ (see Table 1). However, at 37 °C linearity in the Scatchard plot vanishes and an exponentially decaying curve shape can be observed (Figure S5A). The Rosenthal method⁵¹ was applied revealing a slight increase in the total number of binding sites ($N_{T,37} = 9.2 \pm 2.9$). The binding sites can be subdivided into two groups of either strong ($N_{E,37,I} = 4.0 \pm 1.3$) or weak binding sites ($N_{E,37,II} = 5.2 \pm 1.6$). This concept was already described by Karush⁶⁴ for exemplifying cooperativity of ligand binding to albumins which describes the observed processes best. It can be rationalized that the total number of binding sites might slightly change with temperature.

A cooperativity test can be performed according to Tanford¹ that reveals an interesting feature when both Scatchard plots are compared in terms of $\ln K_{A,int}^*$ (Figure S5B, see refs 8,28 for details on the derivation). In principle, the plot of $\ln K_{A,int}^*$ versus N_L yields the concentration-dependent, stepwise energetic contributions of associated ligands. The interpretation is made according to the suggestion of De Meyts and Roth.⁶⁵ At 25 °C, the typical noncooperative (N.C.) region is identified up to $N_L \approx 6.5$, as it was similarly observed for unmodified BSA that is followed by negative cooperativity up to $N_L = 8$. However, at 37 °C, there is a region of negative cooperativity for $N_L < 6.5$, which switches to positive cooperativity above this value. Although the altered behavior at 37 °C might imply activated physiological function, for simplicity and a more precise determination of the total number of binding sites (N_T), CW EPR data at 25 °C may be better suited for standard analyses.

Additionally, a van't Hoff plot of the temperature-dependent association constant K_A can be constructed from data shown in Figure 2C (1.13 equiv of 16-DSA per HSA). In this case we showed that the tight binding regime is valid ($[L]_t < [R]_t = N_T \cdot c_{HSA}$).³⁹ For simplicity, the total receptor concentration in the solution is assumed to remain constant at a value of $[R]_t = 1.46$

mM for all temperatures, as it is only of interest where the strongest change in affinity occurs. Additionally, the bound fraction is here merely derived from the sum of spectral fractions ϕ of dynamic regimes b_1 , b_2 and g ($\phi_b = \phi_{b1} + \phi_{b2} + \phi_g$).

As 16-DSA binding at lower temperatures is so strong that the free (f) fractions are indiscernible from noise ($\phi_{f,5-49} < 0.02\%$) at the start loading ratio used here, a temperature dependent van't Hoff plot of K_A in this temperature range is unfortunately inaccessible (5 °C – 53 °C). However, a fit function can be applied to the $\ln K_{A,j}$ curve above 53 °C as shown in Figure 4B to obtain a better quantitative description of the temperature-dependent ligand binding process. The general shape of $\ln K_{A,j}$ is best described by a Boltzmann function of the kind

$$\ln K_{A,j} = -\ln[N_{T,25} \cdot c_H \left(\frac{[L]_t}{[L]_{b,j} + [L]_{g,j}} \right) - [L]_{f,j}]$$

$$= \alpha_1 + \frac{\alpha_2 - \alpha_1}{(1 + e^{(x-\alpha_3)/\alpha_4})} \quad (1)$$

where α_z ($z = 1-4$) are fit parameters that are given in Table S4. For mathematical clarity, the inverse temperature from the van't Hoff plots is now replaced by $x = T^{-1}$. This description of the ligand association constant K_A contains the initial assumption that HSA denaturation is a hypothetical two-state phase transition, e.g., from a solid (s) to a vapor (v) state.⁶⁶ In literature, nonlinear van't Hoff plots in general were already reported for other systems, too.^{67,68} An assignment of physical meaning to the fit parameters in eq 1 can be developed in the following way: the denaturation process of HSA occurs in a defined temperature range ΔT with a midpoint temperature $T_m = \alpha_3^{-1}$ between the states of energy $H_1 = \alpha_1$ and $H_2 = \alpha_2$.⁶⁹ The respective temperature range $\Delta T = (\alpha_3 - \alpha_4)^{-1} - \alpha_3^{-1} = 6.61$ K of the transition also defines the corresponding slope $k_{KA} = (\alpha_2 - \alpha_1)/(4\Delta T) = 0.155$ K⁻¹ at T_m .^{69,70} The midpoint temperature or melting temperature of HSA is therefore at $T_m = 75.3 \pm 0.9$ °C, as determined from the maximum change in ligand binding affinity. Table 1 reveals that the most affected functional property of HSA upon temperature increase is the decrease of the macroscopic ligand association constant K_A by more than 2 orders of magnitude (~ 200 times, assuming that $N_T = N_{T,25} = 8.1$ at all temperatures). Therefore, the free energy of 16-DSA association also becomes less negative and the observed ligand binding process thus becomes less exergonic ($\Delta G_{A,97}^{\circ} - \Delta G_{A,25}^{\circ} = 7.9$ kJ mol⁻¹).

These data are in very good agreement with results obtained by Gantchev and Shopova,¹⁶ who also reported $N_T = 8 \pm 1$ for HSA. Furthermore, almost identical free energies were found for palmitic acid binding to HSA. Spector et al.⁷¹ also found two classes of binding sites with $\Delta G_{A,37,I}^{\circ} = -39.8$ kJ/mol and $\Delta G_{A,37,II}^{\circ} = -32.2$ kJ/mol. An ITC study by Aki and Yamamoto

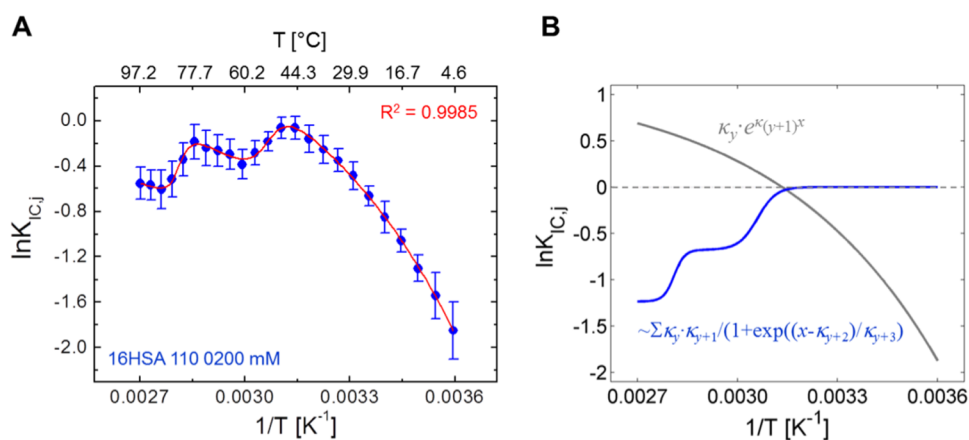


Figure 5. A van't Hoff plot of $\ln K_{IC}$ from 16-DSA bound to HSA. (A) Individual data points of the van't Hoff plot for $\ln K_{IC}$ were calculated from eq 2 with the spectral fractions ϕ_{b1} and ϕ_{b2} of 16-DSA bound to HSA (blue) in the temperature range from 5 to 97 °C. A fit curve derived from eq 3 is shown in red ($R^2 = 0.9985$). (B) Mathematical decomposition and presentation of individual components of the fit function for $\ln K_{IC,j}$ highlighting the second and third term of eq 3.

revealed similar results for palmitic acid interacting with HSA ($\Delta G_{A,37}^\circ = -38.8$ kJ/mol).⁷²

Thermodynamic Analysis of the Interconversion Process of 16-DSA Bound to HSA. After the first EPR-based analysis of FA binding to HSA, now the temperature-dependent interconversion process before and during the denaturation process of HSA is characterized from the bound ligands' point of view and the emerging immobilized spectral fractions (ϕ_{bij} , see³⁹ for further details). Values for $\ln K_{IC}$ are constructed from Figure 2B according to eq 2 ($K_{IC} = \phi_{b2}/\phi_{b1}$) and the corresponding temperature response of the system consisting of 16-DSA bound to HSA is shown in Figure 5.

$$K_{IC,j,k} = \frac{k_{1,j,k}}{k_{-1,j,k}} = \frac{\phi_{b2,j,k}}{\phi_{b1,j,k}} = \frac{\phi_{b2,j,k}}{1 - \phi_{b2,j,k}} = \frac{[L]_{b2,j,k}}{[L]_{b1,j,k}} \quad (2)$$

As shown for core-shell polymers, an arbitrary fit function with the only purpose to reproduce the curve mathematically can be found for the van't Hoff plot of $\ln K_{IC}$ that is given in eq 3 ($x = T^{-1}$). The sum of the exponential second term of eq 3 and a double Boltzmann expression (the complete third term of eq 3 in parentheses) mathematically fits best to describe the temperature-dependent progression of the interconversion equilibrium

$$\ln K_{IC,x} = \ln K_{IC,0} + \kappa_1 \cdot e^{\kappa_2 x} + \left(\frac{\kappa_3 \kappa_4}{1 + e^{(x-\kappa_5)/\kappa_6}} + \frac{\kappa_3(1 - \kappa_4)}{1 + e^{(x-\kappa_7)/\kappa_8}} \right) \quad (3)$$

yielding a correlation coefficient of $R^2 = 0.9985$. Pure polynomial functions fully fail in reproducing this $\ln K_{IC}$ curve shape. All corresponding fit parameter values of $\ln K_{IC,0}$ and κ_y ($y = 1 - 8$) are shown in Table S5. Optionally, the second term $\kappa_1 \cdot \exp(\kappa_2 \cdot x)$ can also be written as a polynomial equation $u \cdot x + v \cdot x^2$. The resulting fit curve of $\ln K_{IC,j}$ and the rationale for separating individual contributions is given in Figure 5. The application of a double Boltzmann term generally implies that two dynamic transitions may occur in HSA that affect the temperature course of $\ln K_{IC,j}$.

The parameters κ_3 and κ_4 can be understood as arbitrary step heights of the transitions and parameters κ_5 and κ_7 are the

midpoint temperatures T_m of the individual transitions, while κ_6 and κ_8 are the individual transition widths. A straightforward thermodynamic analysis can be conducted for $\ln K_{IC}$ of 16-DSA interacting with HSA in accordance to the strategy developed in³⁹ (eqs S8–S34 in the Supporting Information).

The temperature-dependent interconversion enthalpy change is obtained from eq 3 with the relation

$$\Delta H_{IC,x}^\circ = -R \frac{\partial \ln K_{IC,x}}{\partial x} \quad (4)$$

resulting in

$$\Delta H_{IC,x}^\circ = -R \left(\kappa_1 \kappa_2 \cdot e^{\kappa_2 x} - \frac{\kappa_3 \kappa_4}{\kappa_6} \cdot \frac{e^{(x-\kappa_5)/\kappa_6}}{(1 + e^{(x-\kappa_5)/\kappa_6})^2} - \frac{\kappa_3(1 - \kappa_4)}{\kappa_8} \cdot \frac{e^{(x-\kappa_7)/\kappa_8}}{(1 + e^{(x-\kappa_7)/\kappa_8})^2} \right) \quad (5)$$

Together with the relation $\Delta G_{IC}^\circ = \Delta H_{IC}^\circ - T \Delta S_{IC}^\circ = -RT \ln K_{IC}$, at equilibrium the temperature-dependent molar interconversion entropy change may also be determined as

$$\begin{aligned} \Delta S_{IC,x}^\circ &= x \cdot \Delta H_{IC,x}^\circ + R \ln K_{IC,x} \\ &= -R \cdot x \left(\kappa_1 \kappa_2 \cdot e^{\kappa_2 x} - \frac{\kappa_3 \kappa_4}{\kappa_6} \cdot \frac{e^{(x-\kappa_5)/\kappa_6}}{(1 + e^{(x-\kappa_5)/\kappa_6})^2} - \frac{\kappa_3(1 - \kappa_4)}{\kappa_8} \cdot \frac{e^{(x-\kappa_7)/\kappa_8}}{(1 + e^{(x-\kappa_7)/\kappa_8})^2} \right) \\ &\quad + R \left(\ln K_{IC,0} + \kappa_1 \cdot e^{\kappa_2 x} + \frac{\kappa_3 \kappa_4}{1 + e^{(x-\kappa_5)/\kappa_6}} + \frac{\kappa_3(1 - \kappa_4)}{1 + e^{(x-\kappa_7)/\kappa_8}} \right) \end{aligned} \quad (6)$$

As described in the Supporting Information, the differential equation of the molar heat capacity change $\Delta C_{p,IC}^\circ = d\Delta H_{IC}^\circ/dT$ is best calculated by

$$\Delta C_{p,IC,j}^\circ = \left(\frac{\partial \Delta H_{IC,j}^\circ}{\partial T} \right)_p = \frac{1}{T^2} \cdot \left(\frac{\partial \Delta H_{IC,j}^\circ}{\partial \left(\frac{1}{T} \right)} \right)_p \quad (7a)$$

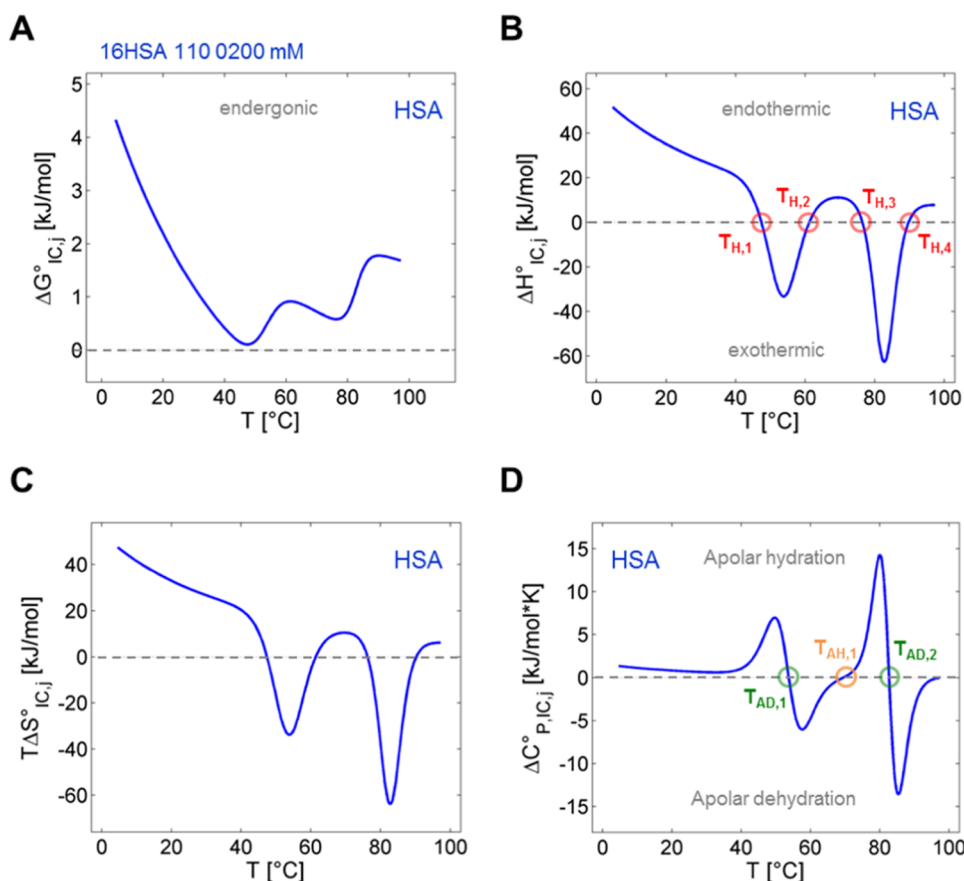


Figure 6. Graphical representation of the thermodynamic functions derived from $\ln K_{IC,j}$ with 16-DSA bound to HSA. Continuous depiction of (A) molar Gibbs free energy change $\Delta G^\circ_{IC,j}$ that remains endergonic in the whole temperature range. (B) Temperature-induced change of molar enthalpy $\Delta H^\circ_{IC,j}$ calculated from eq 5 comprising endothermic and exothermic regions and enthalpy compensation temperatures $T_{H,1} - T_{H,4}$ highlighted with red circles. (C) Temperature-dependent change in molar entropy $T\Delta S^\circ_{IC,j}$ calculated from eq 6. (D) Change in molar heat capacity $\Delta C^\circ_{P,IC,j}$ with apolar dehydration temperatures $T_{AD,1}$ and $T_{AD,2}$ in green and the apolar hydration temperature $T_{AH,1}$ in orange. The corresponding curve was calculated from eq 8. All curves are obtained from the interconversion process $\ln K_{IC,j}$ from data presented in Figures 2B and 5A.

$$\Delta C^\circ_{P,IC,x} = x^2 \cdot \left(\frac{\partial \Delta H^\circ_{IC,x}}{\partial x} \right)_P = -Rx^2 \left(\frac{\partial^2 \ln K_{IC,x}}{\partial x^2} \right)_P \quad (7b)$$

yielding

$$\begin{aligned} \Delta C^\circ_{P,IC,x} = & -Rx^2 \cdot \left(\frac{2\kappa_3\kappa_4}{\kappa_6^2} \cdot \frac{e^{2(x-\kappa_5)/\kappa_6}}{(e^{(x-\kappa_5)/\kappa_6} + 1)^3} \right. \\ & + \frac{2\kappa_3(1-\kappa_4)}{\kappa_8^2} \cdot \frac{e^{2(x-\kappa_7)/\kappa_8}}{(e^{(x-\kappa_7)/\kappa_8} + 1)^3} \\ & - \frac{\kappa_3\kappa_4}{\kappa_6^2} \cdot \frac{e^{(x-\kappa_5)/\kappa_6}}{(e^{(x-\kappa_5)/\kappa_6} + 1)^2} - \frac{\kappa_3(1-\kappa_4)}{\kappa_8^2} \cdot \frac{e^{(x-\kappa_7)/\kappa_8}}{(e^{(x-\kappa_7)/\kappa_8} + 1)^2} \\ & \left. + \kappa_1\kappa_2^2 e^{\kappa_2 x} \right) \end{aligned} \quad (8)$$

Explicit derivations are given in the Supporting Information S6. In Figure 6 all functions are plotted in the full temperature range. Note that the spectral fraction of b_1 does not decrease below $\phi_{b1,j} = 0.5$, thus leading to constantly negative $\ln K_{IC}$ values (Figure 6A). This means that ΔG°_{IC} is always endergonic and the interconversion process is therefore unfavorable throughout the whole observed temperature range. However, the ΔG°_{IC} curve exhibits a global minimum at 47.4 °C, where the free energy approaches zero ($\Delta G^\circ_{IC} \approx 0.11$ kJ/mol).

Intriguingly, this is the temperature region in which also the onset of the HSA expansion, or structural opening, can be observed in the corresponding DLS data of Figure 3D (SLI_{min}). Above 47.4 °C the interconversion process of bound 16-DSA is again more unfavorable.

Unlike Gibbs free energy, the corresponding enthalpy changes ΔH°_{IC} of the interconversion process (Figure 6B) strongly alternate between endothermic and exothermic. Altogether, four enthalpy compensation temperatures are found, $T_{H,1} = 47.4$ °C, $T_{H,2} = 61.1$ °C, $T_{H,3} = 76.5$ °C, and $T_{H,4} = 89.7$ °C. Hence, this process is entropy driven ($\Delta H^\circ_{IC} > 0$, $\Delta S^\circ_{IC} > 0$) and endothermic below 47.4 °C, from 61.1 to 76.5 °C, and above 89.7 °C. In the intervals between 47.4 to 61.1 °C and 76.5 to 89.7 °C the dynamic interconversion process of 16-DSA is enthalpy driven ($\Delta H^\circ_{IC} < 0$, $\Delta S^\circ_{IC} < 0$) and energy is released (exothermic). These characteristic temperatures are summarized in Figure S6 and were calculated according to eqs S35–S37 in the Supporting Information as in.³⁹ Molar entropy changes $T\Delta S^\circ_{IC,j}$ exhibit very analog behavior (Figure 6C).

The changes in molar heat capacity $\Delta C^\circ_{P,IC}$ in Figure 6D reveal a slight apolar hydration ($\Delta C^\circ_{P,IC} > 0$) below 38 °C, before a significant increase is detected with a maximum at 49.7 °C. This is again indicative of an opening of the HSA structure that exposes some hydrophobic regions containing 16-DSA ligands to the solvent. The zero-crossing at $T_{AD,1} = 53.6$ °C terminates the apolar hydration temperature region. Note that

the solvent exposure of hydrophobic regions/ligand coincides with the onset of detectable free ligand fractions ϕ_f and the gel fraction ϕ_g . This means that protein aggregation is triggered and ligand binding becomes less favorable, as it was already shown for core-shell polymers with intermediate-sized hydrophobic cores.³⁹ Accordingly, the structural integrity of HSA is notably deteriorated above $T_{AD,1}$.

This loss in protein structure and functionality is again converted into an apolar hydration process above $T_{AH,1} = 69.4$ °C. This (second) apolar hydration process is much more pronounced than the first one (from about 38 to 53 °C) with a maximum appearing at 80.0 °C. This temperature range (70 to 80 °C) also shows the strongest decrease in HSA's ligand binding affinity (Figure 4B, $\ln K_A$), where the corresponding midpoint temperature is found at $T_m = 75.3 \pm 0.9$ °C. At $T_{AD,2} = 82.7$ °C, apolar dehydration is re-established and the SLI from DLS experiments exhibits the strongest increase. This final apolar dehydration therefore coincides with the formation of larger HSA aggregates (Figure 3C), ultimately leading to macroscopic gelation.

Comparison of Spectroscopic $\ln K_{IC}$ with Results from DSC. The EPR-derived thermodynamic analyses of the ligand-based parameter $\ln K_{IC}$ can be compared to the changes in heat capacity of HSA as observed in DSC experiments. Accordingly, this approach combines nanoscopic thermodynamic properties obtained from the SLFAs' points of view with the macroscopic heat signature of the protein and ligands solution. Thus, samples have been prepared identically, each containing 16-DSA-to-HSA equivalents of 1.1:1.0 at $c_{HSA} = 0.18$ mM. The DSC thermogram in Figure 7 (black) exhibits the classical bimodal appearance of albumin loaded with FAs^{53,73} showing maxima at the two denaturation temperatures $T_{D,1} = 65.1$ °C and $T_{D,2} = 75.1$ °C. This bimodal thermogram was initially interpreted to include a ligand redistribution process during denaturation.^{53,54,74} The FAs released from molten, or denatured HSA

molecules were thought to be absorbed by the remaining intact HSA, contributing their binding energy to internal protein stability.⁵³ This is a common phenomenon in ligand binding to macromolecules.⁷⁵ Here, our EPR-derived thermodynamic data do not reproduce the DSC thermogram shape but rather reveal some of the underlying dynamic processes as observed from EPR in HSA-ligand interconversion. First of all, the two denaturation temperatures $T_{D,i}$ from DSC are not directly found in thermodynamic analyses of $\ln K_{IC}$.

Fit parameters for midpoint temperatures in Figure 5A are identified as the apolar dehydration temperatures $T_{AD,1}$ (κ_5^{-1}) and $T_{AD,2}$ (κ_7^{-1}) that represent zero crossings of $\Delta C_{P,IC,j}^\circ$ roughly coinciding with the onset and end of heat capacity changes in HSA as detected in DSC experiments ($\Delta C_{P,HSA}^\circ$). Consistently, the T_{AD} values give the minima of the ΔH_{IC}° and ΔS_{IC}° curves. However, this direct correlation of DSC and EPR curves reveals that $T_{AH,1}$ is close to the minimum between $T_{D,1}$ and $T_{D,2}$ in the DSC curve, while $T_{H,3}$ almost exactly coincides with the second melting peak ($T_{D,2}$). The enthalpy compensation temperature $T_{H,3}$ also indicates the strongest increase or maximum slope in apolar hydration as observed from $\Delta C_{P,IC}^\circ$ of the ligand interconversion process.

On a more fundamental level, the ligand interconversion changes to endothermic reaction conditions for temperatures between $T_{H,2}$ and $T_{H,3}$, while the first melting peak develops and ceases ($T_{D,1}$). This means that the interconversion process of 16-DSA becomes energetically more favorable during the first phase transition in the HSA substrate when also interconversion entropy $T\Delta S_{IC}^\circ$ rises. This behavior suggests that ligand and protein undergo a mutual energetic coupling, at least to a certain extent.

The conclusion can be drawn that apolar dehydration temperatures T_{AD} from ligand interconversion coincide with fine-tuned structural rearrangements in albumin that trigger denaturation and aggregation. However, both $T_{AD,1}$ and $T_{AD,2}$ in HSA differ from the denaturation temperatures (T_D) and are not detected in DSC experiments as they rather confine the temperature range of the whole biphasic denaturation process (53.6–82.7 °C). In contrast, the apolar hydration temperature $T_{AH,1}$ marks the onset of a transient structural rearrangement that induces an increased structural stability in HSA, even at high temperatures. From an energetic viewpoint, FAs can be seen to absorb heat in form of a favored interconversion and indicate the second melting peak ($T_{D,2}$). The simultaneous increase in interconversion entropy ($T_{AH,1} = 69.4$ °C) illustrates that the ligand obtains additional degrees of motional freedom.

The change in temperature stability upon 16-DSA loading was also investigated by DSC. A typical ligand-induced conversion in the melting behavior (T_D) is seen in Figure 8A ranging from bimodality at lower FA equivalents (up to ca. 5 equiv) to a single melting peak at higher loadings. The relative increase in melting temperatures is depicted in the scheme of Shrake and Ross.⁵³ While the first melting peak ($T_{D,1}$) is shifted linearly upon 16-DSA loading, the second melting peak position ($T_{D,2}$) reaches a plateau value of 75 °C already between 1 and 2 equiv (Figure 8B).

Additionally, the fit functions for T_D give a lower ($T_{D,1,min} = 63.6$ °C) and upper ($T_{D,2,max} = 76.1$ °C) denaturation temperature limit that defines the maximum observed stability increase of $\Delta T_{D,max} = 12.5$ °C as induced by the presence of 16-DSA (Figure 8B). These values are in very good agreement with reported values^{76–78} and—as a side note—also confirm that the commercially available HSA really was largely FA-free.

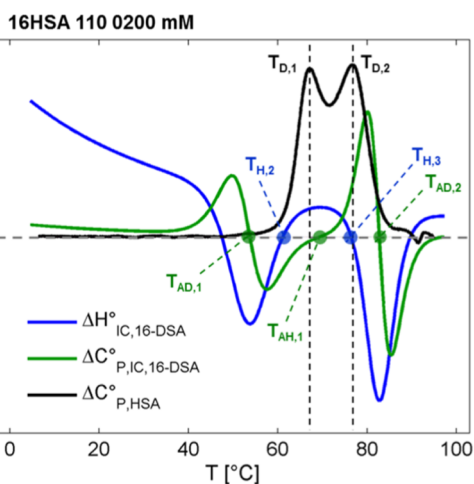


Figure 7. Comparison of $\ln K_{IC}$ thermodynamics with a DSC thermogram of 16-DSA bound to HSA. Here, an overlap of EPR data together with a DSC thermogram is shown that represents heat capacity changes of HSA molecules ($\Delta C_{P,HSA}^\circ$ black) comprising denaturation temperatures $T_{D,1}$ and $T_{D,2}$. EPR data are taken from Figure 6B ($\Delta H_{IC,16-DSA}^\circ$ blue) and Figure 6D ($\Delta C_{P,IC,16-DSA}^\circ$ here green) that highlights 16-DSA-based interconversion enthalpy compensation temperatures $T_{H,2}$ and $T_{H,3}$, as well as changes of ligand hydration at $T_{AD,1}$, $T_{AH,1}$ and $T_{AD,2}$. The exact ligand-to-protein ratio for both methods was 1.1:1.0.

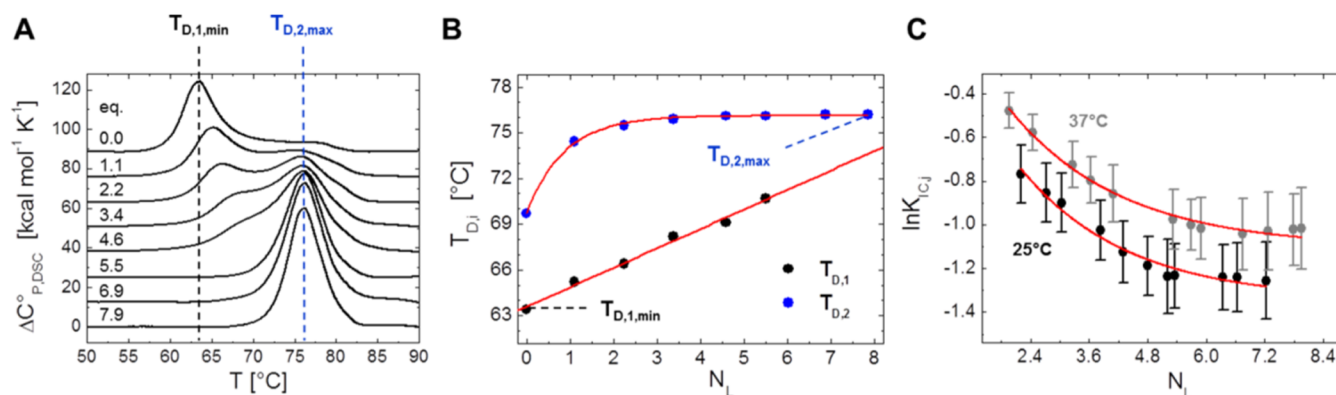


Figure 8. Temperature stability shift of HSA by 16-DSA loading in the view from DSC and EPR. (A) DSC thermograms of HSA loaded in the range from 0 to about 8 FA equivalents. The melting temperatures $T_{D,1,min}$ and $T_{D,2,max}$ represent the minimum and maximum melting temperatures as induced by the absence or presence of 16-DSA, respectively. (B) Melting temperatures $T_{D,1}$ (black) and $T_{D,2}$ (blue) of HSA depending on FA loading equivalents N_L . Individual values are taken from thermograms in (A). Linear (eq S38) and exponential (eq S39) fit curves are shown in red with characteristic values $T_{D,1,min}$ and $T_{D,2,max}$ highlighted. Fit parameters can be found in Table S6. (C) Influence of 16-DSA loading on $\ln K_{IC,j}$ for 25 °C (black) and 37 °C (gray) as derived from EPR spectroscopy. All $\ln K_{IC,j}$ values are taken from simulations that were used for Scatchard plot construction (Figure S4) with respective exponential fit curves according to eq S40 shown in red. Fit parameters can be found in Table S7.

Simulation data from both Scatchard plots (Figure S4) provide a viewpoint on how 16-DSA loading leads to a global shift in the interconversion equilibrium (K_{IC}). Similar to results that are obtained from $T_{D,2}$ in DSC experiments, no further global change in $\ln K_{IC}$ is observed when HSA is loaded with about $N_L \geq 5$ FAs regardless of temperature (Figure 8C). Intriguingly, not only temperature but also 16-DSA loading defines to which extent the interconversion process is endergonic. While a temperature increase shifts this equilibrium to free diffusion (b_2), an increased 16-DSA loading shifts the ligand interconversion back to Brownian diffusion (b_1), i.e., $\ln K_{IC}$ generally decreases when the b_1 fraction increases. Therefore, dynamic ligand interconversion gets more unfavorable with higher FA loading. Hence, fatty acid ligands in general can be truly seen as (negative) temperature equivalents for HSA as they contribute their free energy of binding to protein stability, however, only partially.^{75,79} In this regard, the slope $\partial T_{D,1}/\partial N_L$ from the linear fit to $T_{D,1}$ in Figure 8B gives a value of $k_{TD,1} = 1.28 \pm 0.06$ °C/FA. Thus, the first HSA melting temperature is shifted for about +1.3 K with each additional 16-DSA molecule. Both exponential decays of $\ln K_{IC}$ in Figure 8C exhibit an almost identical decay constant $B_{K_j} = 2.2 \pm 0.3$ FA, indicating independence of temperature. Therefore, temperature (here: $\Delta T = 37$ °C – 25 °C = 12 K) mainly shifts the ligand concentration dependent $\ln K_{IC}$ isotherm along the y -axis. Accordingly, the difference $\Delta \ln K_{IC,\Delta T}$ is assumed to be largely constant for all 16-DSA loadings. This value lies around 0.24 and corresponds to $\Delta \Delta G_{IC}^\circ = 0.48$ kJ/mol, as determined by $\ln K_{IC,0}$ for the plateau at $N_L \rightarrow \infty$ (see also Table S7). We conclude, that FA binding reduces internal flexibility in HSA with a simultaneous gain in temperature stability and indirectly confirms the picture of FAs as “lock pins”.⁷⁷ 16-DSA, or presumably FAs in general, can be seen as natural pharmacological chaperones (“pharmacoperones”), i.e., small molecules that promote refolding of proteins exposed to stress or with dysfunctional mutations.^{80,81}

Further Insights into Ligand Redistribution Using DEER Spectroscopy. In case that the proposed stabilizing ligand redistribution⁵⁴ takes place during temperature-induced HSA denaturation, the binding site occupation of the remaining intact proteins should change to a certain extent. Using DEER

spectroscopy, we have established the “fingerprint” distribution of FA binding sites, of the “entry points” to the sites on the protein’s surface as well as to the anchor points (amino acid binding site) in its interior.^{3,6,41–43} Furthermore, we found that for BSA in solution the characteristic FA distributions coincided very well with the ones expected from the crystal structure (of BSA and HSA), while for HSA this is only true for its interior – the entry point distribution of FAs strongly deviates from the crystal structure.^{3,6,41,43} Yet, the entry site distribution in HSA is remarkably simple (less anisotropic) and is essentially bimodal with distance peaks at 2.2 and 3.6 nm.^{3,41} We here use an empirical analysis of the ratio of these two peaks in direct dependence of the solution temperature before shock-freezing the samples. This is necessary for DEER experiments with nitroxide radicals, which have to be carried out at cryogenic temperatures (here: 50 K). Therefore, small amounts of cryoprotectants like glycerol have to be added to guarantee vitrification of the temperature-induced albumin ensemble^{3,82} and associated changes in the subdomains.

Characterization of Ligand Redistribution Using DEER Spectroscopy. CW EPR results have shown that a strong decrease in binding affinity toward 16-DSA takes place at temperatures above 53 °C, which indicates the release and redistribution process of bound ligands during HSA denaturation but does not allow one to locate the remaining binding sites. In Figure S5 it is furthermore shown that binding site cooperativity changes with temperature and we have tested whether 4-pulse DEER can provide further insights into the redistribution, or interconversion process.

It was already shown in Junk et al.⁴² that HSA exhibits much smaller modulation depths for a 16-DSA loading ratio of 2:1 than derived from model biradicals, despite a similar number of coupled spins should be present. Therefore, standard spin counting procedures that utilize standardized inversion efficiencies λ do not apply properly for this self-assembled system. Another study also emphasizes the effect that cooperativity may have on modulation depth.⁸³ Furthermore, the potential number of accessible binding sites in this study (here: $N_T = 8.1 \pm 0.3$, see Table 1) gives rise to tremendous multispin effects that leads to overestimation of short distances and suppression of large distances. First, the previous experi-

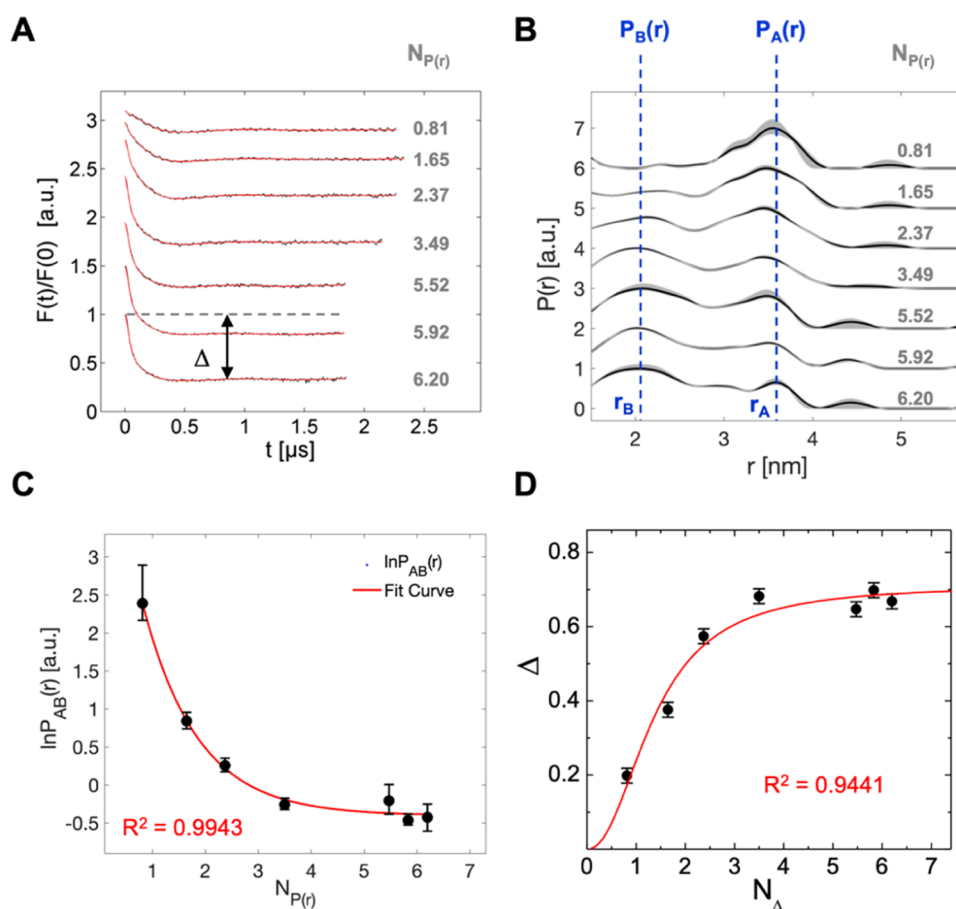


Figure 9. Effect of ligand loading in DEER data for 16-DSA-probed HSA solutions. HSA was loaded with 16-DSA equivalents from 0.81 – 6.20 at $c_{\text{HSA}} = 0.18$ mM. (A) Corresponding dipolar evolution functions $F(t)/F(0)$, regularized fits (red), modulation depths Δ (gray dotted line, indicated for highest loading ratio 6.2) and (B) resulting distance distributions $P(r)$. The two most prominent features in $P(r)$ are denoted as $P_A(r)$ at $r_A = 3.5 \pm 0.1$ nm and $P_B(r)$ at about $r_B = 2.2 \pm 0.2$ nm. The validated distance distributions $P(r)$ were determined with DeerAnalysis2019. Confidence intervals of all $P(r)$ curves are given as gray shaded areas. (C) Data points for $\ln P_{AB}(r)$ (black dots) are shown as a function of 16-DSA concentration equivalents $N_{P(r)}$. An exponential fit curve (red) is applied to the $\ln P_{AB}(r)$ curve (red) that finally yields eq 9. Asymmetric error bars were extracted as variations from values of $P_A(r)$ and $P_B(r)$ in $P(r)$ curves in (B). (D) The modulation depths Δ are presented as a function of 16-DSA equivalents N_{Δ} (black dots) with a fit curve (red) corresponding to eq 10. Both fit curves in (C) and (D) show high correlation coefficients with $R^2 > 0.94$.

ments from Junk et al.⁴² are here similarly reproduced with the 16-DSA-probed HSA system (here in equivalents of $c_{\text{HSA}} = 0.18$ mM). In an initial step, CW EPR was applied on an aliquot from the final DEER sample in order to determine the true FA concentration in the sample solution by double integration (Figure S7A).

As it was shown in,⁸⁴ all binding pockets are occupied to a certain extent in the solution ensemble of HSA, even at a 1:1 loading ratio. This is indirectly confirmed by the Scatchard plot at 25 °C in Figure 4A giving $N_{T,25} = 8.1 \pm 0.3$ equiv, noncooperative binding sites. Even at the highest loading ratios of about 1:7 ($N_L \approx 7$), more than 98.5% of supplied 16-DSA remains bound to HSA.

The corresponding DEER measurements of each CW EPR sample exhibit the well-known increase in modulation depths up to values of about $\Delta \approx 0.7$ (Figure 9A). The resulting distance distributions in Figure 9B also exhibit an overestimation of short distances to quite some extent for $N_L > 2$, as it was shown in.⁴² The main characteristics of these 16-DSA-derived distance distributions are now termed as $P_A(r)$ for the peak at $r_A = 3.5 \pm 0.1$ nm and $P_B(r)$ for the peak at $r_B = 2.2 \pm 0.2$ nm that are used for the construction of the relative intensity ratio $P_{AB}(r) = P_A(r)/P_B(r)$. As this $P_{AB}(r)$ value may cover a wide range of

several orders of magnitude, it is depicted as its natural logarithm in Figure 9C ($\ln P_{AB}(r)$). Generally, the first moment or average distance value $\langle r \rangle$ of the complete distance distribution can be used as an assessment measure for rather broad and ambiguous distance distributions.^{52,85} This first moment $\langle r \rangle$ does not only contain information about the weight center of $P(r)$, but also reflects slight shifts of r_A and r_B for up to about 0.4 nm that might indicate allosteric reorganizations of individual binding pockets upon 16-DSA ligand loading.^{5,62,86} The above-described lock-pin behavior has been reported to increase the albumin diameter by about 0.5 nm through a relative rotation of domains I and II.⁶² Instead, this effect is here observed as a general decrease of FA interspin distances acting like a shoelace that ties the domains together. Hence, $\ln P_{AB}(r)$ mainly represents the rise in relative intensity changes of $P_B(r)$, depending on the number of equivalent 16-DSA molecules per HSA. A quite smooth curve is obtained for $\ln P_{AB}(r)$ that can be fitted with an exponential function (eq S41 in the SI). From these data, an empirical formula can be derived that correlates $\ln P_{AB}(r)$ with the FA content $N_{P(r)}$ by

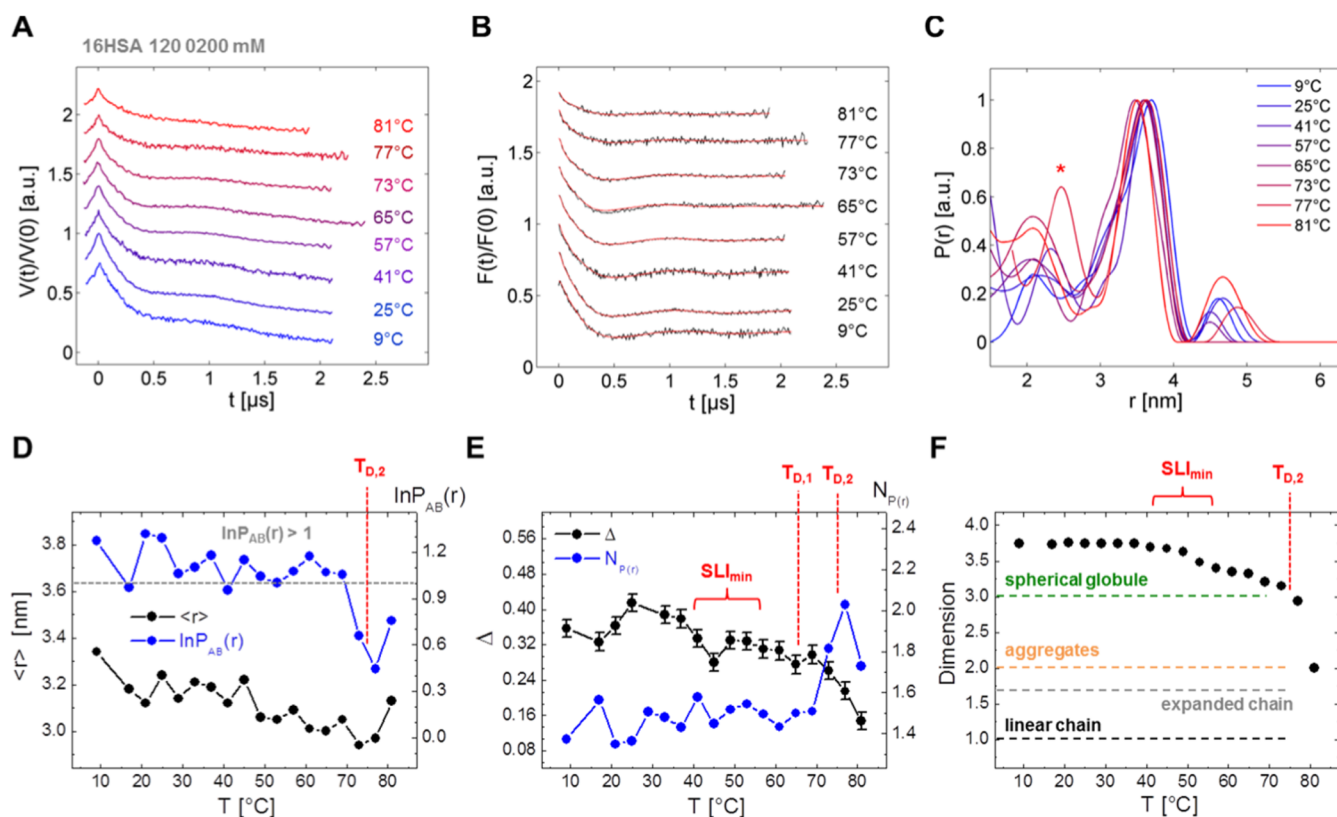


Figure 10. DEER results from temperature denaturation of 16-DSA-probed HSA solutions. (A) Several temperature-dependent raw DEER time traces $V(t)/V(0)$ of 16-DSA-probed HSA (2:1), incubated at selected temperatures with corresponding (B) dipolar evolution functions $F(t)/F(0)$ (black) with regularized fit curves (red) and (C) distance distributions $P(r)$. The red asterisk in (C) highlights the distribution shape at 77 °C. (D) The first moments $\langle r \rangle$ (black) of $P(r)$ and $\ln P_{AB}(r)$ (blue) are shown as functions of temperature. The gray dotted line indicates $\ln P_{AB}(r) = 1$. (E) Experimental modulation depths Δ and $N_{P(r)}$ (from eq 9) are presented as functions of temperature. Error bars for individual modulation depths were chosen as $\Delta\Delta = 0.02$ as suggested in Bode et al.⁸⁸ (F) Temperature-dependent background dimensionality change of 16-DSA-probed HSA. The different typical dimensionality regimes are denoted to indicate shapes of homogeneous and spherical globules ($D = 3$), aggregates/oligomers ($D = 2$), expanded chains ($D = 1.67$) and linear chains.^{44,52} The red items in D–F indicate $T_{D,1} = 65.5$ °C as the first and $T_{D,2} = 74.9$ °C as the second melting temperature from DSC results, calculated from eqs S38 and S39 in the Supporting Information, the corresponding loading ratio is $N_{P(r)} = 1.47$. SLI_{min} is here given as the temperature range from DLS data in Figure 3D where HSA elongates and the subdomains are assumed to decouple.

$$N_{P(r)} = -\ln\left(\frac{20 \cdot \ln P_{AB}(r) + 9}{17 \cdot N_{T,25}}\right) \quad (9)$$

where $\ln P_{AB}(r)$ is the experimental parameter from the distance distribution. A quick and intuitive derivation of eq 9 and fit parameters are shown in the Supporting Information (Table S8). The modulation depth Δ also increases in a nonlinear fashion to a saturation-like state above $N_{\Delta} > 3.5$ (Figure 9D). A mathematical model is here adopted for 16-DSA adsorption to HSA (eq 10) in analogy to a Langmuir isotherm that is usually applied to describe gas absorption to energetically heterogeneous surfaces⁸⁷

$$\Delta = \frac{\Delta_{max} \cdot b \cdot N_{\Delta}^{\eta}}{1 + b \cdot N_{\Delta}^{\eta}} \quad (10)$$

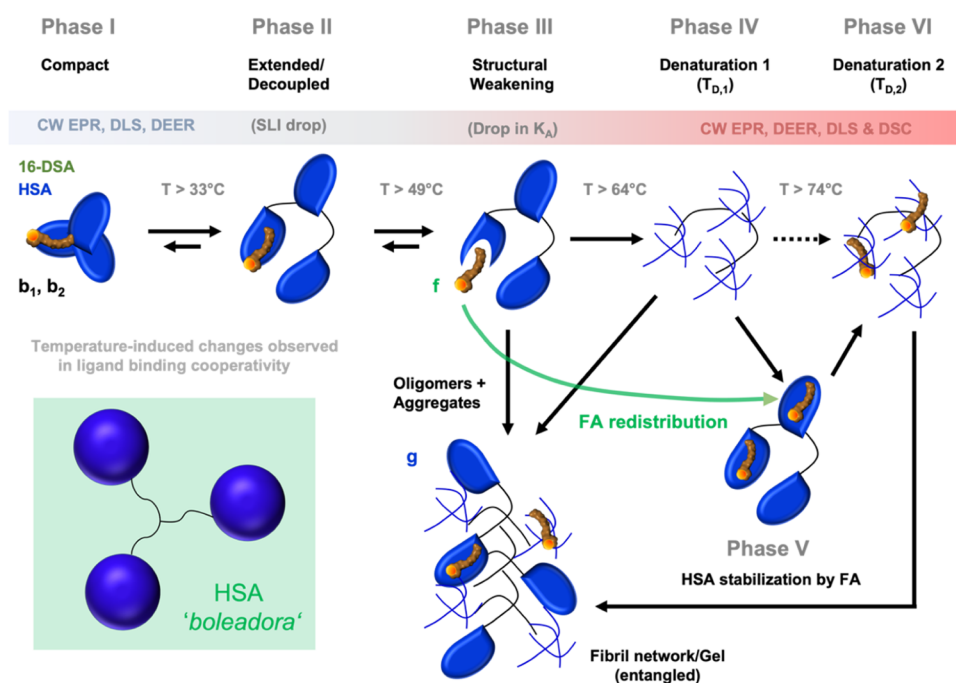
Thus, the number of 16-DSA molecules that are absorbed by HSA can be determined by modulation depths from DEER experiments using the following empirical expression

$$N_{\Delta} = \left(\frac{\Delta}{b \cdot (\Delta_{max} - \Delta)}\right)^{1/\eta} \quad (11)$$

Mathematically, the parameters $b = 0.503$ and $\Delta_{max} = 0.712$ (see Table S9) are equivalent to the Langmuir constants, and $\eta = 2.203$ is a stretching factor that originally considers energetic inhomogeneities on absorbing surfaces. In our application eq 11 directly correlates modulation depth to the number of occupied ligand binding sites of each HSA molecule.

However, these spin counting strategies are intrinsically restricted and are only applicable in the range of about $0 < N_L < 4$ equiv of 16-DSA due to the saturation-like behavior in the corresponding $\ln P_{AB}(r)$ and modulation depth (Δ) curves (Figure 9C,D). Thus, in combination with double integration in CW EPR, eqs 9 and 11 allow for spin counting in an empirical fashion, without accounting for multispin contributions stemming from more than two dipolar-coupled spins in the relevant distance range, which we have studied in HSA before.⁴²

To check for the proposed ligand redistribution processes above 64 °C⁵³ we chose a rather unconventional strategy whose feasibility will be demonstrated in the following. Aliquots from a single 16-DSA-probed HSA stock solution were incubated for 5 min at a respective temperature between 9 and 81 °C. If cooling proceeds in equilibrium with the environment, all ensembles should be identical and should reflect the ensemble at the glass-transition temperature. We chose shock-freezing from the respective temperature directly—a nonequilibrium process to

Scheme 1. Temperature-Induced Dynamic Phases in HSA Solutions Containing 16-DSA^a

^aA Model Was Devised from Available Data in this Study that also Corroborates Prevalent Literature. The Temperature-Dependent Behavior can be Separated in Six Phases (I–VI), whereas the First Three Phases Belong to the Proposed Boleadora-Type Dynamics Model of Globular HSA (Phase I). HSA Elongates/Decouples to a Kind of Boleadora-like Appearance for $T > 33\text{ }^{\circ}\text{C}$ (Phase II), Decreases in Structural Integrity that Leads to a Drop in K_A (f) and the Formation of a Fibril Network/Gel Phase for $T > 49\text{ }^{\circ}\text{C}$ (g , Phase III). During the Transition from Phase I to Phase II, Changes in Ligand Binding Cooperativity can be Observed. The Presentation of the Fibril Network is Shown as Proposed by Bhattacharya et al.⁹⁶ The First Denaturation Phase Occurs in Phase IV above $64\text{ }^{\circ}\text{C}$. The Still Intact HSA Molecule Fraction can be Further Stabilized (Phase V) by Uptake of the FA Ligands that are Released from Denatured HSA Molecules during Phase III and Phase IV. Above $74\text{ }^{\circ}\text{C}$ All HSA Proteins Are Denatured and Accumulate in the Gel Phase (Phase VI).

achieve freezing in a spin ensemble that might be representative of a snapshot of the ensemble at the respective incubation temperature. The results from these experiments are shown in Figure 10. At first sight, the DEER time traces and dipolar evolution functions in Figure 10A,B do not seem to change considerably upon heating. A further interesting aspect is that also the distance distributions do not change decisively (Figure 10C), not even for higher temperatures. However, close inspection of the general distribution shape reveals a slight but traceable increase in $P_B(r)$. Thus, the empirical rules of thumb in eqs 9 and 11 are now applied. The resulting values of $\ln P_{AB}(r)$ are shown in Figure 10D.

An average value of $\ln P_{AB}(r) = 1.13 \pm 0.12$ is obtained as a fingerprint for “native” HSA between ~ 9 to $65\text{ }^{\circ}\text{C}$. Additionally, individual data points are almost entirely located above $\ln P_{AB}(r) > 1$, i.e., when the relative peak ratio is $P_{AB}(r) \approx 3$. Above $70\text{ }^{\circ}\text{C}$, all $\ln P_{AB}(r) < 1$, indicating an increase of the $P_B(r)$ feature in the range of 73 to $81\text{ }^{\circ}\text{C}$, as marked with an asterisk in Figure 10C. The minimum value for $\ln P_{AB}(r)$ is found at $77\text{ }^{\circ}\text{C}$ indicating a maximum intensity in $P_B(r)$, almost perfectly coinciding with $T_{D,2}$ from DSC experiments. In contrast, the first moment $\langle r \rangle$ of $P(r)$ does not show significant changes apart from a slight decrease in the course of HSA temperature denaturation.

The calculation of individual, temperature-dependent $N_{P(r)}$ values is carried out according to eq 9 and is shown in Figure 10E. An average value of $N_{P(r)} = 1.47 \pm 0.07$ is obtained in the temperature range from 9 to $65\text{ }^{\circ}\text{C}$. Like for $\ln P_{AB}(r)$, the maximum number $N_{P(r),\text{max}} = 2.03$ of 16-DSA ligands per HSA is found at $77\text{ }^{\circ}\text{C}$. This must now be associated with an increase in

FA loading in the still intact HSA molecules, or associated binding sites as caused by ligand redistribution. The fit curves of the DSC-derived melting peaks in Figure 8B deliver corresponding 16-DSA melting peak positions ($T_{D,1} = 65.5\text{ }^{\circ}\text{C}$ and $T_{D,2} = 74.9\text{ }^{\circ}\text{C}$) which are also denoted in Figure 10D–F.

While the $N_{P(r)}$ and $\ln P_{AB}(r)$ have features coinciding with $T_{D,2}$ quite well, the temperature-dependent modulation depths only show subtle features. An overall maximum modulation depth of $\Delta = 0.41$ is found at $25\text{ }^{\circ}\text{C}$ and at $45\text{ }^{\circ}\text{C}$ a first local minimum appears in the temperature range that coincides with the drop in SLI from DLS experiments ($\text{SLI}_{\text{min}} \approx 40 - 55\text{ }^{\circ}\text{C}$) reflecting the loss in protein compactness. A slight kink is also seen for $T_{D,1}$. For $T > 70\text{ }^{\circ}\text{C}$, Δ significantly decreases steadily after passing $T_{D,2}$ indicating transient loss toward total loss of HSA compactness or at least an increased contribution of unmodulated background. This can be seen as being caused by the release of ligands, or the ongoing transition from well-defined strongly interacting to more loose and flexible binding states. It would be of interest to analyze whether the same effects occur when the DOXYL group is located deeper inside of the binding tunnel, namely by exchanging the spin probe 16-DSA by 5-DSA.

The background dimensionality of the raw DEER time traces was also adjusted carefully to extract additional qualitative information. A typical value of $D = 3.74$ could be used for HSA at lower incubation temperatures ($T < 40\text{ }^{\circ}\text{C}$).^{3,41,44} As this parameter is sensitive to changes in global shape and excluded volume,⁴⁴ successful analyses of available DEER data are only possible when dimensionality is adjusted between 3.0 and 3.7 for

temperatures between 40 and 70 °C. Besides the sharp dimensionality drop beyond $T_{D,2}$ ($D < 3$), indicating transition to more linearly stretched albumin polypeptide chains,^{44,89} data evaluation is strongly hampered and proper spin echo formation vanishes, likely due to denatured protein in gel-like fractions (see also Figure 2C).⁷ Inhomogeneous vitrification due to protein denaturation from incubations above 81 °C render DEER experiments increasingly inaccessible. Note that the dimensionality curve in Figure 10F resembles an inverted SLI curve (Figure 3D).

CONCLUSIONS

The observed dynamic processes from 16-DSA-probed HSA solutions in EPR spectroscopy, DLS and DSC are summarized in Scheme 1 (loading ratio 1:1). Overall, six different dynamic rearrangement phases of HSA are encountered in this study. The compact and native state of HSA is clearly observed in the temperature range from about 5 to 40 °C and is termed as Phase I. At $T > 33$ °C the protein structure starts to extend as detected by a drop in scattered light intensity (SLI) in DLS experiments (Figure 3D). Simultaneously, the Brownian diffusion component b_1 in corresponding EPR spectra shows a nonlinear decrease in rotational correlation times (Figure 3A), unlike the free diffusion component b_2 . Both applied methods, CW EPR and DLS, confirm a protein-based structural extension or decoupling mechanism without any detectable phase transition in DSC. This phenomenon in Phase II can be described as a *rotational decoupling of domains* in HSA, leading to a *boleadora*-type domain arrangement. This temperature-induced domain decoupling was proposed in several other studies,^{90,91} usually referred to as going along with mild alterations in secondary structure.^{60,61} The existence of a ligand-independent opened and closed state of albumin⁹² cannot be confirmed from the obtained data, as the time scale of this process (300 ms) by far exceeds the nanosecond time scale.⁹³ However, the energetic contributions from FA binding to HSA (Figure 6) are quite similar to values that were reported in the kinetic model of a two-step attachment profile given by Scheider.⁹⁴

In phase III, the ligand association constant K_A experiences a detectable drop above 53 °C as the HSA molecule shows increased FA release (f), indicative of a structural weakening. At the same time a gel fraction (g) appears in CW EPR spectra, formed by aggregation of individual proteins as confirmed by a spontaneous increase in SLI at this temperature. It is noteworthy that Banerjee and Pal⁹⁵ found a structural transition in BSA at 54 °C by differential thermal analysis (DTA) that could be also related to slight changes in DLS data. Altogether, four coexisting dynamic components are observed in CW EPR spectra of 16-DSA (b_1 , b_2 , f and g) with the onset of phase III. The rotational decoupling model can be reconciled with the structural elongation/weakening of HSA in a *boleadora*-type picture. We suggest that this is the reason for a mutual entanglement of (sub)domains, as they accumulate and form gel-like, water-depleted regions that are here probed by amphiphilic 16-DSA ligands. Phase IV sets in above 64 °C and denotes the first denaturation process of HSA ($T_{D,1}$). While a fraction of HSA is denatured, 16-DSA release is amplified accordingly.

This emerging free fraction of ligand is now assumed to be absorbed by still intact HSA molecules, however, with lower affinity, leading to a structural stabilization (Phase V) of the still functional HSA molecules. Therefore, these proteins experience a shift in denaturation temperatures $T_{D,i}$ (Figure 8B) as a consequence of the pharmacoperone property⁸¹ of the FAs

(Phase VI). Finally, after oligomerization sets in via self-capturing HSA boleadoras, ultimately a macroscopic gel is formed that consists of a mixture of denatured protein and intact (sub)domains still harboring 16-DSA ligands.

It is also intriguing that the observed phenomena recur in data from diverse methods. Changes in rotational correlation times in CW EPR coincide with SLI effects in DLS data, as well as changes in hydrodynamic radii ($R_{H,j}$). Additionally, even DEER data exhibit sensitivities to these observed hydrodynamic effects in CW EPR and DLS.

Besides the modulation depth (Δ) that can be viewed as a measure of the overall compactness of the protein ensemble (Figure 10E), the background dimensionality (D) qualitatively resembles an inverted shape of the SLI curve from DLS results (Figures 3D and 10F). In particular CW EPR data reveal sophisticated properties in the interconversion thermodynamics that indirectly reflect phase transitions as obtained from DSC, however, on the nanoscopic level of ligand solvation. In this study, it was thus shown that the strategies that were developed for the calculation of interconversion processes (K_{IC}) in core-shell polymers can also contribute to a better nanothermodynamic understanding of much more complex systems such as HSA.

Ligand hydration states can clearly be obtained from $\Delta C_{p,IC}$. As it was predicted earlier, such hydration interactions exhibit complicated temperature dependences of ΔC_p .⁹⁷ This is in line with the findings made here (Figure 7). The obtained apolar dehydration temperatures $T_{AD,1} = 53.6$ °C and $T_{AD,2} = 82.7$ °C denote the onset and the termination of the denaturation process in HSA. Furthermore, the region around the apolar hydration temperature $T_{AH,1} = 69.4$ °C most probably describes the thermodynamically stabilizing process by ligand reorganization in the system that ultimately leads to the appearance of a second denaturation temperature $T_{D,2}$ (Figure 8). The derived thermodynamic quantities show how intricately ligands and protein are energetically coupled. In particular, the heat capacity curves of HSA ($\Delta C_{p,HSA}^\circ$, from DSC) and 16-DSA interconversion ($\Delta C_{p,IC}^\circ$, from CW EPR), respectively, are almost directly complementary.

The predicted second denaturation temperature from DSC experiments ($T_{D,2} = 74.4$ °C) coincides quite well with the value obtained from the van't Hoff plot of $\ln K_A$ ($T_m = 75.3 \pm 0.9$ °C) for identical loading ratios (1.13 equiv of 16-DSA). With increasing 16-DSA:HSA ratio, $\ln K_{IC}$ from CW EPR data (Figure 8C), Δ from DEER data (Figure 9D), and $T_{D,2}$ from DSC experiments (Figure 8B) all reach a plateau value, indicating that structural stabilization experiences a saturation at about $3.5 < N_L < 5.0$ bound FA equivalents. An ITC study of Fang et al.⁹⁸ revealed that only 5 binding sites contribute to structural changes that accompany FA binding (in this case: myristate). From all this, one may conclude that these plateau-like regions above $N_L > 3.5$ illustrate allosteric reorganizations of HSA reducing its flexibility. Experimental parameters $\ln K_{IC}$, Δ , and also SLI values can be seen to truly probe for protein compactness and flexibility. The bound (paramagnetic) FAs can be understood as effective intrinsic melting temperature-increasing equivalents ($T_{D,1,min} + 1.28 \text{ }^\circ\text{C} \cdot N_L$). These FAs contribute to HSA's stability solely upon binding and are therefore considered as physiological pharmacoperones.

DEER data gave experimental evidence for FA ligand redistribution at higher temperatures. This effect leads to a slight, yet detectable change in distance distribution character-

istics ($\ln P_{AB}(r)$) and is indicative of higher ligand binding site occupation per natively folded albumin (ca. +40%).

Our data and the discussion in light of previous knowledge suggest that the established but simple picture of weak and strong binding sites in HSA has to be extended and revised. We suggest that protein compactness strongly affects the mode of diffusion of bound ligand. It has to be further ascertained to which extent ligand binding cooperativity is affected by the rotational decoupling of HSA subdomains. From Figure 4A and SSA it appears as if not only temperature, but also the associated domain proximity has an effect on the nature of ligand binding cooperativity. A similar temperature effect was also observed in laurate and myristate binding to HSA by Pedersen et al.⁹⁹ The FA-lock pin hypothesis given by Curry⁶² can be confirmed by $\ln K_{IC}$ at different 16-DSA loadings and temperatures (Figure 8C).

In summary, it should be emphasized that the stability of HSA is not only induced by the sheer presence of FA ligands, but is also energetically driven from the interconvertible modes of intrinsic FA diffusion that facilitate storage of thermal energy in form of rotational entropy. As we have described, e.g., in gel formation in HSA and BSA can take place below the denaturation temperature. The boleadora-type rotational model visualizes the partial unfolding into three rotationally decoupled domains that then interact and finally lead to protein entanglement and gel formation.

In future studies, we will transfer this EPR-spectroscopic approach to other ligand binding proteins and especially test whether the pharmacoperone-activity of bound ligands is observable and potentially functionally important there, too. This will include proteins of the FA binding protein (FABP) family, for which we have observed interconversion of prebinding and strong binding of FAs.¹⁰⁰

■ ASSOCIATED CONTENT

SI Supporting Information

The Supporting Information is available free of charge at <https://pubs.acs.org/doi/10.1021/acs.jpcb.4c08717>.

Further Sample Preparation Details, Determination of the Critical Micelle Concentration (CMC) of 16-DSA, CW EPR Simulations and Parameters, Scatchard Plot Construction, Fit Parameters of $\ln K_{IC}$ of 16-DSA bound to HSA, Derivation of Thermodynamic Functions of $\ln K_{IC}$, Fitting Function from Temperature Stability Shifts in DSC and $\ln K_{IC}$, Spin Counting and Fitting Functions from DEER-derived Parameters $\ln P_{AB}(r)$ and Δ as Functions of 16-DSA Loading (PDF)

■ AUTHOR INFORMATION

Corresponding Author

Dariush Hinderberger – Institute of Chemistry, Physical Chemistry – Complex Self-Organizing Systems, Martin Luther University Halle-Wittenberg, 06120 Halle (Saale), Germany; orcid.org/0000-0002-6066-7099; Email: dariush.hinderberger@chemie.uni-halle.de

Authors

Jörg Reichenwallner – Institute of Chemistry, Physical Chemistry – Complex Self-Organizing Systems, Martin Luther University Halle-Wittenberg, 06120 Halle (Saale), Germany; Department of Biochemistry, University of Toronto, Toronto, Ontario M5S 1A8, Canada

Sebastian Michler – Institute of Chemistry, Physical Chemistry – Complex Self-Organizing Systems, Martin Luther University Halle-Wittenberg, 06120 Halle (Saale), Germany

Christian Schwieger – Institute of Chemistry, Physical Chemistry – Complex Self-Organizing Systems, Martin Luther University Halle-Wittenberg, 06120 Halle (Saale), Germany;

orcid.org/0000-0001-8327-1233

Complete contact information is available at:

<https://pubs.acs.org/doi/10.1021/acs.jpcb.4c08717>

Notes

The authors declare no competing financial interest.

■ ACKNOWLEDGMENTS

We thank Heike Schimm and Annetrin Schiebel for continuing technical support. This project was funded by the Deutsche Forschungsgemeinschaft (DFG, German Research foundation) - project-ID 436494874 - RTG 2670 'Beyond Amphiphilicity (BEAM)' *The authors would like to dedicate this publication to Hans Wolfgang Spiess, Max Planck Institute for Polymer Research, Mainz, Germany, for his generous and general support and mentorship throughout the time of when this study has been conceived and data generated.*

■ REFERENCES

- (1) Tanford, C. *Physical Chemistry of Macromolecules*; John Wiley & Sons, 1961.
- (2) Spector, A. A. Fatty-Acid Binding to Plasma Albumin. *J. Lipid Res.* **1975**, *16* (3), 165–179.
- (3) Reichenwallner, J.; Hinderberger, D. Using bound fatty acids to disclose the functional structure of serum albumin. *Biochim. Biophys. Acta* **2013**, *1830* (12), 5382–5393.
- (4) Peters, Jr., T. *All about Albumin: Biochemistry, Genetics and Medical Applications*; Academic Press, Inc.: San Diego, 1995.
- (5) Ascenzi, P.; Fasano, M. Allostery in a monomeric protein: The case of human serum albumin. *Biophys. Chem.* **2010**, *148* (1–3), 16–22.
- (6) Akdogan, Y.; Reichenwallner, J.; Hinderberger, D. Evidence for water-tuned structural differences in proteins: an approach emphasizing variations in local hydrophilicity. *PLoS One* **2012**, *7* (9), No. e45681.
- (7) Arabi, S. H.; Aghelnejad, B.; Schwieger, C.; Meister, A.; Kerth, A.; Hinderberger, D. Serum albumin hydrogels in broad pH and temperature ranges: characterization of their self-assembled structures and nanoscopic and macroscopic properties. *Biomater. Sci.* **2018**, *6* (3), 478–492.
- (8) Reichenwallner, J.; Thomas, A.; Steinbach, T.; Eisermann, J.; Schmelzer, C. E. H.; Wurm, F.; Hinderberger, D. Ligand-Binding Cooperativity Effects in Polymer-Protein Conjugation. *Biomacromolecules* **2019**, *20* (2), 1118–1131.
- (9) Wallach, D. F. H.; Verma, S. P.; Weidekamm, E.; Bieri, V. Hydrophobic Binding-Sites in Bovine Serum-Albumin and Erythrocyte Ghost Proteins - Study by Spin-Labeling, Paramagnetic Fluorescence Quenching and Chemical Modification. *Biochim. Biophys. Acta* **1974**, *356* (1), 68–81.
- (10) Morrisett, J. D.; Pownall, H. J.; Gotto, A. M., Jr. Bovine serum albumin. Study of the fatty acid and steroid binding sites using spin-labeled lipids. *J. Biol. Chem.* **1975**, *250* (7), 2487–2494.
- (11) Kuznetsov, A. N.; Ebert, B.; Lassmann, G.; Shapiro, A. B. Adsorption of Small Molecules to Bovine Serum-Albumin Studied by Spin-Probe Method. *Biochim. Biophys. Acta* **1975**, *379* (1), 139–146.
- (12) Heinrich Ruf, H.; Gratzl, M. Binding of Nitroxide Stearate Spin Labels to Bovine Serum-Albumin. *Biochim. Biophys. Acta* **1976**, *446* (1), 134–142.
- (13) Rehfeld, S. J.; Eatough, D. J.; Plachy, W. Z. Binding Isotherms for Interaction of 5-Doxyl Stearic-Acid with Bovine and Human-Albumin. *J. Lipid Res.* **1978**, *19* (7), 841–849.

- (14) Abumrad, N. A.; Perkins, R. C.; Park, J. H.; Park, C. R. Mechanism of Long-Chain Fatty-Acid Permeation in the Isolated Adipocyte. *J. Biol. Chem.* **1981**, *256* (17), 9183–9191.
- (15) Perkins, R. C.; Abumrad, N.; Balasubramanian, K.; Dalton, L. R.; Beth, A. H.; Park, J. H.; Park, C. R. Equilibrium Binding of Spin-Labeled Fatty-Acids to Bovine Serum-Albumin - Suitability as Surrogate Ligands for Natural Fatty-Acids. *Biochemistry* **1982**, *21* (17), 4059–4064.
- (16) Gantchev, T. G.; Shopova, M. B. Characterization of Spin-Labeled Fatty-Acids and Hematoporphyrin Binding-Sites Interactions in Serum-Albumin. *Biochim. Biophys. Acta* **1990**, *1037* (3), 422–434.
- (17) Shenkar, M. G.; Rananavare, S. B.; Freed, J. H. ESR studies of stearic acid binding to bovine serum albumin. *Biochim. Biophys. Acta* **1990**, *1036* (3), 228–236.
- (18) Gaffney, B. J.; McConnell, H. M. Paramagnetic-Resonance Spectra of Spin Labels in Phospholipid Membranes. *J. Magn. Reson.* **1974**, *16* (1), 1–28.
- (19) Kazmierczak, S. C.; Gurachevsky, A.; Matthes, G.; Muravsky, V. Electron spin resonance spectroscopy of serum albumin: A novel new test for cancer diagnosis and monitoring. *Clin. Chem.* **2006**, *52* (11), 2129–2134.
- (20) Gurachevsky, A.; Shimanovitch, E.; Gurachevskaya, T.; Muravsky, V. Intra-albumin migration of bound fatty acid probed by spin label ESR. *Biochem. Biophys. Res. Commun.* **2007**, *360* (4), 852–856.
- (21) de Sousa Neto, D.; Salmon, C. E.; Alonso, A.; Tabak, M. Interaction of bovine serum albumin (BSA) with ionic surfactants evaluated by electron paramagnetic resonance (EPR) spectroscopy. *Colloids Surf. B Biointerfaces* **2009**, *70* (1), 147–156.
- (22) Schmidt, C.; Krumbiegel, C.; Waterstradt, K.; Petznick, G.; Schafer, H.; Schnurr, K. Expectation-maximization-estimation of mixture densities for Electron-Spin-Resonance-analysis of albumin. In *IEEE International Workshop on Genomic Signal Processing and Statistics, Minneapolis, MN, USA, 2009*.
- (23) Anjos, J. L. V.; Santiago, P. S.; Tabak, M.; Alonso, A. On the interaction of bovine serum albumin with ionic surfactants: temperature induced EPR changes of a maleimide nitroxide reflect local protein dynamics and probe solvent accessibility. *Colloids Surf. B Biointerfaces* **2011**, *88* (1), 463–470.
- (24) Pavićević, A.; Luo, J. H.; Popovic-Bijelic, A.; Mojovic, M. Maleimido-proxyl as an EPR spin label for the evaluation of conformational changes of albumin. *Eur. Biophys. J.* **2017**, *46* (8), 773–787.
- (25) Akdogan, Y.; Emrullahoglu, M.; Tatlidil, D.; Ucuncu, M.; Cakan-Akdogan, G. EPR studies of intermolecular interactions and competitive binding of drugs in a drug-BSA binding model. *Phys. Chem. Chem. Phys.* **2016**, *18* (32), 22531–22539.
- (26) Hauenschild, T.; Reichenwallner, J.; Enkelmann, V.; Hinderberger, D. Characterizing Active Pharmaceutical Ingredient Binding to Human Serum Albumin by Spin-Labeling and EPR Spectroscopy. *Chem.—Eur. J.* **2016**, *22* (36), 12825–12838.
- (27) Pavićević, A. A.; Popovic-Bijelic, A. D.; Mojovic, M. D.; Susnjar, S. V.; Bacic, G. G. Binding of doxyl stearic spin labels to human serum albumin: an EPR study. *J. Phys. Chem. B* **2014**, *118* (37), 10898–10905.
- (28) Henning, C.; Stübner, C.; Arabi, S. H.; Reichenwallner, J.; Hinderberger, D.; Fiedler, R.; Girndt, M.; Di Sanzo, S.; Ori, A.; Glomb, M. A. Glycation Alters the Fatty Acid Binding Capacity of Human Serum Albumin. *J. Agric. Food Chem.* **2022**, *70* (9), 3033–3046.
- (29) Gurachevsky, A.; Muravskaya, E.; Gurachevskaya, T.; Smirnova, L.; Muravsky, V. Cancer-associated alteration in fatty acid binding to albumin studied by spin-label electron spin resonance. *Cancer Invest.* **2007**, *25* (6), 378–383.
- (30) Matthes, G.; Seibt, G.; Muravsky, V.; Hersmann, G.; Dornheim, G. Albumin transport analysis of different collected and processed plasma products by electron spin resonance spectroscopy. *Transfus. Apher. Sci.* **2002**, *27* (2), 129–135.
- (31) Muravsky, V.; Gurachevskaya, T.; Berezhenko, S.; Schnurr, K.; Gurachevsky, A. Fatty acid binding sites of human and bovine albumins: differences observed by spin probe ESR. *Spectrochim Acta A Mol. Biomol. Spectrosc.* **2009**, *74* (1), 42–47.
- (32) Gelos, M.; Hinderberger, D.; Welsing, E.; Belting, J.; Schnurr, K.; Mann, B. Analysis of albumin fatty acid binding capacity in patients with benign and malignant colorectal diseases using electron spin resonance (ESR) spectroscopy. *Int. J. Colorectal Dis.* **2010**, *25* (1), 119–127.
- (33) Alonso, A.; dos Santos, W. P.; Leonor, S. J.; dos Santos, J. G.; Tabak, M. Stratum corneum protein dynamics as evaluated by a spin-label maleimide derivative: effect of urea. *Biophys. J.* **2001**, *81* (6), 3566–3576.
- (34) Alonso, A.; Vasques da Silva, J.; Tabak, M. Hydration effects on the protein dynamics in stratum corneum as evaluated by EPR spectroscopy. *Biochim. Biophys. Acta* **2003**, *1646* (1–2), 32–41.
- (35) Kuan, S. L.; Stockle, B.; Reichenwallner, J.; Ng, D. Y.; Wu, Y.; Doroshenko, M.; Koynov, K.; Hinderberger, D.; Mullen, K.; Weil, T. Dendronized albumin core-shell transporters with high drug loading capacity. *Biomacromolecules* **2013**, *14* (2), 367–376.
- (36) Tatlidil, D.; Ucuncu, M.; Akdogan, Y. Physiological concentrations of albumin favor drug binding. *Phys. Chem. Chem. Phys.* **2015**, *17* (35), 22678–22685.
- (37) Strancar, J.; Koklic, T.; Arsov, Z.; Filipic, B.; Stopar, D.; Hemminga, M. A. Spin label EPR-based characterization of biosystem complexity. *J. Chem. Inf. Model.* **2005**, *45* (2), 394–406.
- (38) Reichenwallner, J.; Thomas, A.; Nuhn, L.; Johann, T.; Meister, A.; Frey, H.; Hinderberger, D. Tunable dynamic hydrophobic attachment of guest molecules in amphiphilic core-shell polymers. *Polym. Chem.* **2016**, *7* (37), 5783–5798.
- (39) Reichenwallner, J.; Schwiager, C.; Hinderberger, D. Probing the Nanoscopic Thermodynamic Fingerprint of Paramagnetic Ligands Interacting with Amphiphilic Macromolecules. *Polymers* **2017**, *9* (8), 324.
- (40) Curry, S.; Brick, P.; Franks, N. P. Fatty acid binding to human serum albumin: new insights from crystallographic studies. *Biochim. Biophys. Acta* **1999**, *1441* (2–3), 131–140.
- (41) Junk, M. J. N.; Spiess, H. W.; Hinderberger, D. The distribution of fatty acids reveals the functional structure of human serum albumin. *Angew. Chem., Int. Ed.* **2010**, *49* (46), 8755–8759.
- (42) Junk, M. J.; Spiess, H. W.; Hinderberger, D. DEER in biological multispin-systems: a case study on the fatty acid binding to human serum albumin. *J. Magn. Reson.* **2011**, *210* (2), 210–217.
- (43) Reichenwallner, J.; Oehmichen, M. T.; Schmelzer, C. E. H.; Hauenschild, T.; Kerth, A.; Hinderberger, D. Exploring the pH-Induced Functional Phase Space of Human Serum Albumin by EPR Spectroscopy. *Magnetochemistry* **2018**, *4* (4), 47.
- (44) Kattinig, D. R.; Reichenwallner, J.; Hinderberger, D. Modeling Excluded Volume Effects for the Faithful Description of the Background Signal in Double Electron-Electron Resonance. *J. Phys. Chem. B* **2013**, *117* (51), 16542–16557.
- (45) Bhattacharya, A. A.; Grune, T.; Curry, S. Crystallographic analysis reveals common modes of binding of medium and long-chain fatty acids to human serum albumin. *J. Mol. Biol.* **2000**, *303* (5), 721–732.
- (46) Dulbecco, R.; Vogt, M. Plaque Formation and Isolation of Pure Lines with Poliomyelitis Viruses. *J. Exp. Med.* **1954**, *99* (2), 167–182.
- (47) Wu, F.; Gaffney, B. J. Dynamic behavior of fatty acid spin labels within a binding site of soybean lipoxygenase-1. *Biochemistry* **2006**, *45* (41), 12510–12518.
- (48) Martin, R. E.; Pannier, M.; Diederich, F.; Gramlich, V.; Hubrich, M.; Spiess, H. W. Determination of End-to-End Distances in a Series of TEMPO Diradicals of up to 2.8 nm Length with a New Four-Pulse Double Electron Resonance Experiment. *Angew. Chem., Int. Ed.* **1998**, *37*, 2833–2837.
- (49) Pannier, M.; Veit, S.; Godt, A.; Jeschke, G.; Spiess, H. W. Dead-time free measurement of dipole-dipole interactions between electron spins. *J. Magn. Reson.* **2000**, *142* (2), 331–340.
- (50) Stoll, S.; Schweiger, A. EasySpin, a comprehensive software package for spectral simulation and analysis in EPR. *J. Magn. Reson.* **2006**, *178* (1), 42–55.

- (51) Rosenthal, H. E. A Graphic Method for Determination and Presentation of Binding Parameters in a Complex System. *Anal. Biochem.* **1967**, *20* (3), 525–532.
- (52) Jeschke, G.; Chechik, V.; Ionita, P.; Godt, A.; Zimmermann, H.; Banham, J.; Timmel, C. R.; Hilger, D.; Jung, H. DeerAnalysis2006 - a comprehensive software package for analyzing pulsed ELDOR data. *Appl. Magn. Reson.* **2006**, *30* (3–4), 473–498.
- (53) Shrake, A.; Ross, P. D. Biphasic denaturation of human albumin due to ligand redistribution during unfolding. *J. Biol. Chem.* **1988**, *263* (30), 15392–15399.
- (54) Shrake, A.; Ross, P. D. Origins and consequences of ligand-induced multiphasic thermal protein denaturation. *Biopolymers* **1992**, *32* (8), 925–940.
- (55) Arabi, S. H.; Aghelnejad, B.; Volmer, J.; Hinderberger, D. Hydrogels from serum albumin in a molten globule-like state. *Protein Sci.* **2020**, *29* (12), 2459–2467.
- (56) Juárez, J.; Taboada, P.; Goy-López, S.; Cambón, A.; Madec, M. B.; Yeates, S. G.; Mosquera, V. Additional Supra-Self-Assembly of Human Serum Albumin under Amyloid-Like-Forming Solution Conditions. *J. Phys. Chem. B* **2009**, *113* (36), 12391–12399.
- (57) Sanaeifar, N.; Mäder, K.; Hinderberger, D. Nanoscopic Characterization of Stearic Acid Release from Bovine Serum Albumin Hydrogels. *Macromol. Biosci.* **2020**, *20* (8), No. 2000126.
- (58) Earle, K. A.; Budil, D. E.; Freed, J. H. 250-GHz EPR of Nitroxides in the Slow-Motional Regime - Models of Rotational Diffusion. *J. Phys. Chem. A* **1993**, *97* (50), 13289–13297.
- (59) Freed, J. H. Theory of slow tumbling ESR spectra for nitroxides. In *Spin Labeling: Theory and Applications*; Berliner E, L. J., Ed.; Academic Press: New York, 1976; Vol. 1, pp 53–132.
- (60) Rezaei-Tavirani, M.; Moghaddamnia, S. H.; Ranjbar, B.; Amani, M.; Marashi, S. A. Conformational study of human serum albumin in pre-denaturation temperatures by differential scanning calorimetry, circular dichroism and UV spectroscopy. *BMB Rep.* **2006**, *39* (5), 530–536.
- (61) Mitra, R. K.; Sinha, S. S.; Pal, S. K. Hydration in protein folding: Thermal unfolding/refolding of human serum albumin. *Langmuir* **2007**, *23* (20), 10224–10229.
- (62) Curry, S. Beyond expansion: Structural studies on the transport roles of human serum albumin. *Vox Sang.* **2002**, *83*, 315–319.
- (63) Scatchard, G. The Attractions of Proteins for Small Molecules and Ions. *Ann. Ny Acad. Sci.* **1949**, *51* (4), 660–672.
- (64) Karush, F. Heterogeneity of the Binding Sites of Bovine Serum Albumin. *J. Am. Chem. Soc.* **1950**, *72* (6), 2705–2713.
- (65) De Meyts, P.; Roth, J. Cooperativity in ligand binding: a new graphic analysis. *Biochem. Biophys. Res. Commun.* **1975**, *66* (4), 1118–1126.
- (66) Pande, V. S.; Rokhsar, D. S. Is the molten globule a third phase of proteins? *Proc. Natl. Acad. Sci. U.S.A.* **1998**, *95* (4), 1490–1494.
- (67) Lima, E. C.; Gomes, A. A.; Tran, H. N. Comparison of the nonlinear and linear forms of the van't Hoff equation for calculation of adsorption thermodynamic parameters (ΔS° and ΔH°). *J. Mol. Liq.* **2020**, *311*, No. 113315.
- (68) Tanase, M.; Soare, A.; David, V.; Moldoveanu, S. C. Sources of Nonlinear van't Hoff Temperature Dependence in High-Performance Liquid Chromatography. *ACS Omega* **2019**, *4* (22), 19808–19817.
- (69) Finkelstein, A. V.; Ptitsyn, O. B. *Protein Physics: A Course of Lectures*; Academic Press: London, 2002.
- (70) Saboury, A. A.; Moosavi-Movahedi, A. A. Clarification of calorimetric and van't Hoff enthalpies for evaluation of protein transition states. *Biochem. Educ.* **1994**, *22*, 210–211.
- (71) Spector, A. A.; John, K.; Fletcher, J. E. Binding of long-chain fatty acids to bovine serum albumin. *J. Lipid Res.* **1969**, *10* (1), 56–67.
- (72) Aki, H.; Yamamoto, M. Thermodynamic characterization of drug binding to human serum albumin by isothermal titration microcalorimetry. *J. Pharm. Sci.* **1994**, *83* (12), 1712–1716.
- (73) Gumpen, S.; Hegg, P. O.; Martens, H. Thermal stability of fatty acid-serum albumin complexes studied by differential scanning calorimetry. *Biochim. Biophys. Acta* **1979**, *574* (2), 189–196.
- (74) Shrake, A.; Ross, P. D. Ligand-induced biphasic protein denaturation. *J. Biol. Chem.* **1990**, *265* (9), 5055–5059.
- (75) McGhee, J. D. Theoretical calculations of the helix-coil transition of DNA in the presence of large, cooperatively binding ligands. *Biopolymers* **1976**, *15* (7), 1345–1375.
- (76) Farruggia, B.; Pico, G. A. Thermodynamic features of the chemical and thermal denaturations of human serum albumin. *Int. J. Biol. Macromol.* **1999**, *26* (5), 317–323.
- (77) Picó, G. A. Thermodynamic features of the thermal unfolding of human serum albumin. *Int. J. Biol. Macromol.* **1997**, *20* (1), 63–73.
- (78) Lang, B. E.; Cole, K. D. Unfolding properties of recombinant human serum albumin products are due to bioprocessing steps. *Biotechnol. Prog.* **2015**, *31* (1), 62–69.
- (79) Schellman, J. A. Macromolecular Binding. *Biopolymers* **1975**, *14* (5), 999–1018.
- (80) Janovick, J. A.; Goulet, M.; Bush, E.; Greer, J.; Wettlaufer, D. G.; Conn, P. M. Structure-activity relations of successful pharmacologic chaperones for rescue of naturally occurring and manufactured mutants of the gonadotropin-releasing hormone receptor. *J. Pharmacol. Exp. Ther.* **2003**, *305* (2), 608–614.
- (81) Janovick, J. A.; Stewart, M. D.; Jacob, D.; Martin, L. D.; Deng, J. M.; Stewart, C. A.; Wang, Y.; Cornea, A.; Chavali, L.; Lopez, S.; et al. Restoration of testis function in hypogonadotropic hypogonadal mice harboring a misfolded GnRHR mutant by pharmacoperone drug therapy. *Proc. Natl. Acad. Sci. U. S. A.* **2013**, *110* (52), 21030–21035.
- (82) Hunold, J.; Eisermann, J.; Brehm, M.; Hinderberger, D. Characterization of Aqueous Lower-Polarity Solvation Shells Around Amphiphilic 2,2,6,6-Tetramethylpiperidine-1-oxyl Radicals in Water. *J. Phys. Chem. B* **2020**, *124* (39), 8601–8609.
- (83) Giannoulis, A.; Ackermann, K.; Spindler, P. E.; Higgins, C.; Cordes, D. B.; Slawin, A. M. Z.; Prisner, T. F.; Bode, B. E. Nitroxide-nitroxide and nitroxide-metal distance measurements in transition metal complexes with two or three paramagnetic centres give access to thermodynamic and kinetic stabilities. *Phys. Chem. Chem. Phys.* **2018**, *20* (16), 11196–11205.
- (84) Reichenwallner, J.; Hauenschild, T.; Schmelzer, C. E. H.; Hülsmann, M.; Godt, A.; Hinderberger, D. Fatty Acid Triangulation in Albumins Using a Landmark Spin Label. *Isr. J. Chem.* **2019**, *59* (11–12), 1059–1074.
- (85) Jeschke, G.; Panek, G.; Godt, A.; Bender, A.; Paulsen, H. Data analysis procedures for pulse ELDOR measurements of broad distance distributions. *Appl. Magn. Reson.* **2004**, *26* (1–2), 223–244.
- (86) Ghuman, J.; Zunszain, P. A.; Petipas, L.; Bhattacharya, A. A.; Otigiri, M.; Curry, S. Structural basis of the drug-binding specificity of human serum albumin. *J. Mol. Biol.* **2005**, *353* (1), 38–52.
- (87) Kapoor, A.; Ritter, J. A.; Yang, R. T. An Extended Langmuir Model for Adsorption of Gas-Mixtures on Heterogeneous Surfaces. *Langmuir* **1990**, *6* (3), 660–664.
- (88) Bode, B. E.; Margraf, D.; Plackmeyer, J.; Dürner, G.; Prisner, T. F.; Schiemann, O. Counting the monomers in nanometer-sized oligomers by pulsed electron-electron double resonance. *J. Am. Chem. Soc.* **2007**, *129* (21), 6736–6745.
- (89) Hinderberger, D.; Spiess, H. W.; Jeschke, G. Dynamics, site binding, and distribution of counterions in polyelectrolyte solutions studied by electron paramagnetic resonance spectroscopy. *J. Phys. Chem. B* **2004**, *108* (12), 3698–3704.
- (90) McCarty, T. A.; Page, P. M.; Baker, G. A.; Bright, F. V. Behavior of acrylodan-labeled human serum albumin dissolved in ionic liquids. *Ind. Eng. Chem. Res.* **2008**, *47* (3), 560–569.
- (91) Page, T. A.; Kraut, N. D.; Page, P. M.; Baker, G. A.; Bright, F. V. Dynamics of Loop 1 of Domain I in Human Serum Albumin When Dissolved in Ionic Liquids. *J. Phys. Chem. B* **2009**, *113* (38), 12825–12830.
- (92) Livshits, V. A.; Marsh, D. Fatty acid binding sites of serum albumin probed by non-linear spin-label EPR. *Biochim. Biophys. Acta, Biomembr.* **2000**, *1466* (1–2), 350–360.
- (93) Scheider, W. Ligand-Independent Activated State of Serum-Albumin for Fatty-Acid Binding. *J. Phys. Chem. A* **1980**, *84* (8), 925–928.

(94) Scheider, W. Rate of Access to the Organic Ligand-Binding Region of Serum-Albumin Is Entropy Controlled. *Proc. Natl. Acad. Sci. U.S.A.* **1979**, *76* (5), 2283–2287.

(95) Banerjee, D.; Pal, S. K. Molecular recognition in partially folded states of a transporter protein: Temperature-dependent specificity of bovine serum albumin. *Photochem. Photobiol.* **2008**, *84* (3), 750–757.

(96) Bhattacharya, M.; Jain, N.; Mukhopadhyay, S. Insights into the Mechanism of Aggregation and Fibril Formation from Bovine Serum Albumin. *J. Phys. Chem. B* **2011**, *115* (14), 4195–4205.

(97) Cooper, A. Heat capacity effects in protein folding and ligand binding: a re-evaluation of the role of water in biomolecular thermodynamics. *Biophys. Chem.* **2005**, *115* (2–3), 89–97.

(98) Fang, Y.; Tong, G. C.; Means, G. E. Structural changes accompanying human serum albumin's binding of fatty acids are concerted. *Biochim. Biophys. Acta* **2006**, *1764* (2), 285–291.

(99) Pedersen, A. O.; Honore, B.; Brodersen, R. Thermodynamic Parameters for Binding of Fatty-Acids to Human Serum-Albumin. *Eur. J. Biochem.* **1990**, *190* (3), 497–502.

(100) Michler, S.; Schoffmann, F. A.; Robaa, D.; Volmer, J.; Hinderberger, D. Fatty acid binding to the human transport proteins FABP3, FABP4, and FABP5 from a Ligand's perspective. *J. Biol. Chem.* **2024**, *300* (6), No. 107396.